Draft v0.3.1

CEPC Reference Detector

Technical Design Report

Version: 0.3.1 build: 2025-07-10 19:57:43+08:00

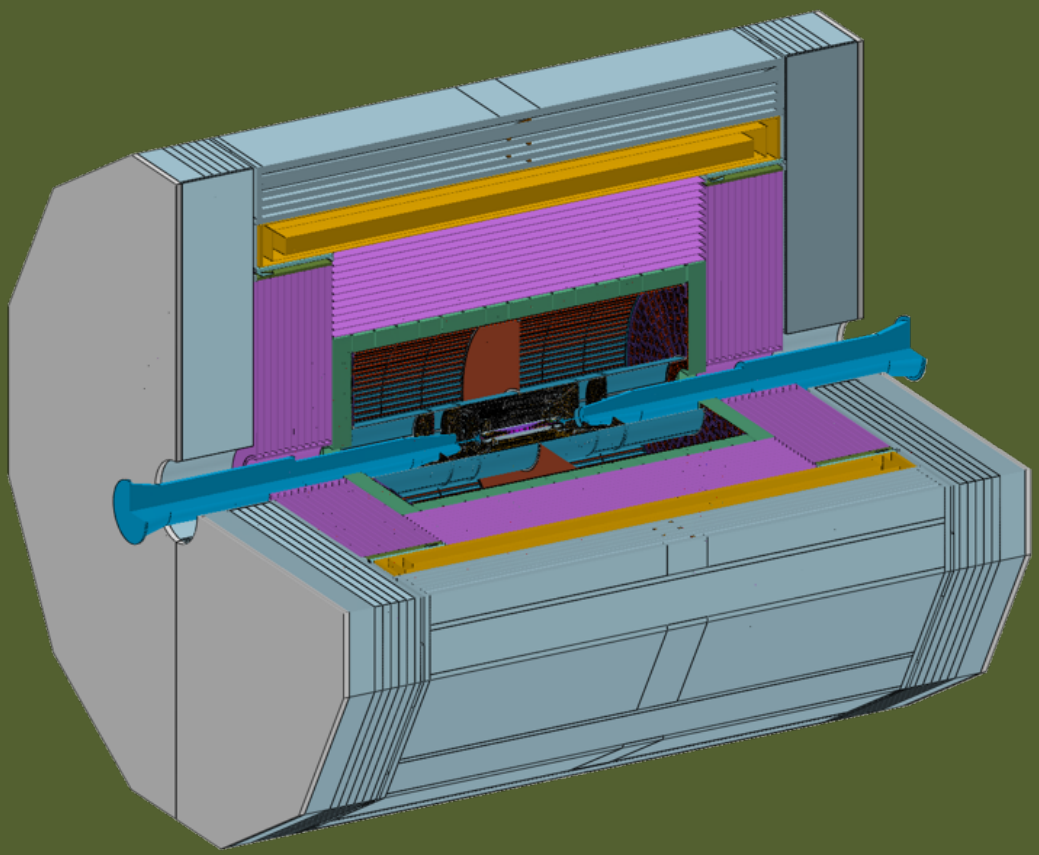

Draft v0.3.1

Contents

Draft v0.3.1

Chapter 4 Vertex Detector

The Circular Electron Positron Collider (CEPC) vertex detector is a crucial component of the tracking system, designed to provide excellent spatial resolution and ultra-low material budget for precision vertexing and flavor tagging. A high-granularity low-mass design based on Monolithic Active Pixel Sensor (MAPS) has been proposed and selected as the CEPC Vertex Detector (VTX) baseline, ensuring high tracking performance without compromising the calorimeter and timing detector coverage.

The CEPC vertex detector is built as six concentric cylindrical pixel layers stretching from a radius of 11 mm to 40 mm around the beam pipe. In the inner four layers, ultra-thin stitched Complementary Metal Oxide Semiconductor (CMOS) sensors are thinned to 40 µm and gently bent to the required curvature, so that each layer forms a seamless half-cylinder. Conventional ladder designs with CMOS sensors mounted on both sides are used for layers 5 and 6. All layers share a common 65 nm MAPS front-end that integrates amplification, discrimination and zero suppression in-pixel, achieving less than 5 µm single-point resolution with a time stamp precision of 100 ns. A stitched "Repeated Sensor Unit" is the building block of the curved chips, maximising wafer utilisation. Average power density is about $38\mathrm{mW/cm^2}$ in the pixel matrix, comfortably under the $40\mathrm{mW/cm^2}$ cm air-cooling limit.

This chapter is organised as: the overall design considerations are outlined in Section 4.1, followed by the design on detector layout along with estimates of the background rate and radiation dose in this layout. Detailed sensor and readout technologies are presented in Section 4.2, Mechanics and cooling design as well as service design are presented in Section 4.3. R&D of key technology are presented in Section 4.5 to support the baseline design of the CEPC vertex detector. The detailed simulation of expected detector performance and detector alignment strategy are presented in Section 4.6. Finally, The summary and future plan are presented in Section 4.7.

4.1 Detector overall design

4.1.1 Vertex detector design specification

The CEPC is designed to operate at high collision frequencies, accommodating multiple collision modes. In its initial 10 years, the plan includes running at 240 GeV in the Higgs boson factory mode and at 90 GeV in the Z boson factory mode. Specifically, the collision frequency for the Higgs factory is approximately 1.7 MHz, while the Z boson factory mode operates at about 14.5 MHz during the initial low-luminosity phase and increases to 43 MHz in the later high-luminosity phase. These frequencies posing

Draft v0.3.1

challenges in maintaining low power consumption at higher operational frequencies - a critical aspect of the vertex detector chip development for this project. The CEPC vertex detector is designed with a power consumption limit of below 40 mW/cm^2 while maintaining a time stamp precision within 100 ns for recorded hits. Additionally, the physics goals of CEPC require the vertex detector to achieve higher spatial resolution, targeting levels close to 3 μm, and to maintain a low material budget of less than 0.15% X_0 per layer. This capability is essential for studying the properties of the Higgs particle, particularly its decay channels involving bottom and charm quarks, and for exploring potential new physics phenomena. In summary, the key requirements are listed in Table 4.1:

Table 4.1: Physics Requirements

Parameter	**Baseline Requirement**
Spatial Resolution	5 μm
Material Budget per Layer	$\leq 0.15\% X_0$
Angular Coverage	$\lvert\cos\theta\rvert < 0.99$

To meet the requirements of low power consumption, low material budget, and high spatial resolution listed in Table 4.1, the MAPS is adopted as the sensor type for the vertex detector. Preliminary simulations and tests based on the first CEPC vertex detector prototype indicate that the power consumption at low-luminosity Z mode operation for the 180 nm technology is larger than 60 mW/cm^2. This level of power dissipation exceeds the air cooling capacity of the vertex detector, resulting in sensor temperatures surpassing the operational upper limit of 30 °C, which may introduce higher noise levels and accelerate the aging of sensors, mechanical components, and other associated systems. To address this critical issue, the vertex detector has adopted 65 nm technology as the baseline technology. This choice significantly reduces power consumption and also offers the potential for smaller pixel sizes, thereby enhancing spatial resolution. In summary, the design parameters are listed in Table 4.2:

Table 4.2: Vertex Detector Design Parameters

Parameter	**Design**
Spatial Resolution	$\leq$5 μm
Material Budget per Layer	$\leq 0.15\% X_0$
Power Consumption	$<$ 40mW/cm^2 (air cooling requirement)
Time stamp precision	$\pm$ 100 ns
Fluence	$\sim 2 \times 10^{14}$Neq/cm^2 (for first 10 years)
Operation Temperature	$\sim$ 5°C to 30°C
Readout Electronics	Fast, low-noise, low-power
Mechanical Support	Ultralight structures
Angular Coverage	$\lvert\cos\theta\rvert < 0.99$

Draft v0.3.1

4.1.2 Detector layout

Based on the requirements of the vertex detector, the vertex detector consists of six layers, covering the pole angle of 8.1°, and is located within the range of 11∼40 mm. Leveraging the existing chip design schemes for the vertex detector, stitching CMOS technology, and planar CMOS technology, the design of the first four layers and the last two layers of the vertex detector is completed. Using traditional planar CMOS technology, each chip is fixed on both sides of the support along the beam direction (z-direction) to form a ladder structure. At a determined radial position, identical ladder structures are arranged sequentially around the z-direction to form the last two layers of the vertex detector, named Planar Vertex Layer (PVTX). The application of stitching technology significantly reduces the total material budget of the vertex detector, with only the first four layers utilizing this technology. The corresponding layers are named the Curved Vertex Layer (CVTX). Two identical sensors of a specific size designed for this layer are bent in the ϕ-direction and then stitched along the z-direction to form a cylindrical surface. The size and number of sensors used in each layer are determined by the radial position of that layer in the vertex detector.

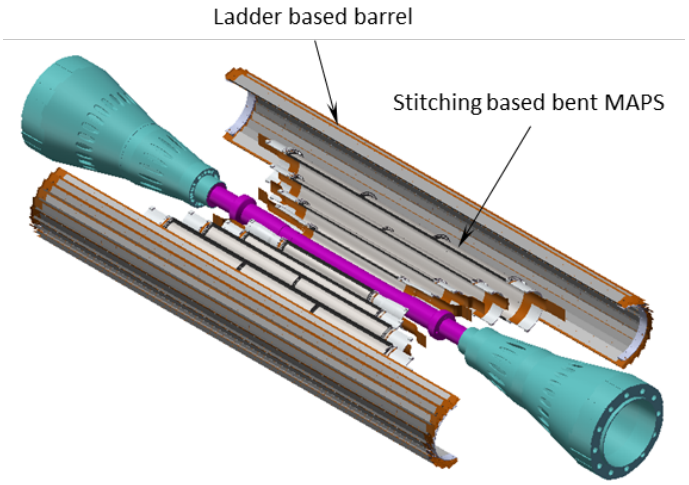

Figure 4.1: Diagram of the vertex detector. The first four layers are designed as single-layer structures (full-model cylindrical structure) using bent stitched sensors, while the last two layers are designed as double-layer structures (ladder structure) utilizing planar CMOS sensors.

Stitching design For the sensors constituting the Curved Vertex Layer (CVTX) of the vertex detector, the length of the bent sensor along the ϕ-direction corresponds to the arc length of a semicircle with a specific radius determined by the CVTX. To achieve the required polar angle coverage of 8.1°, the length of the sensor's sensitive region along the beam direction (z-direction) is also precisely defined. Due to limitations in current

Draft v0.3.1

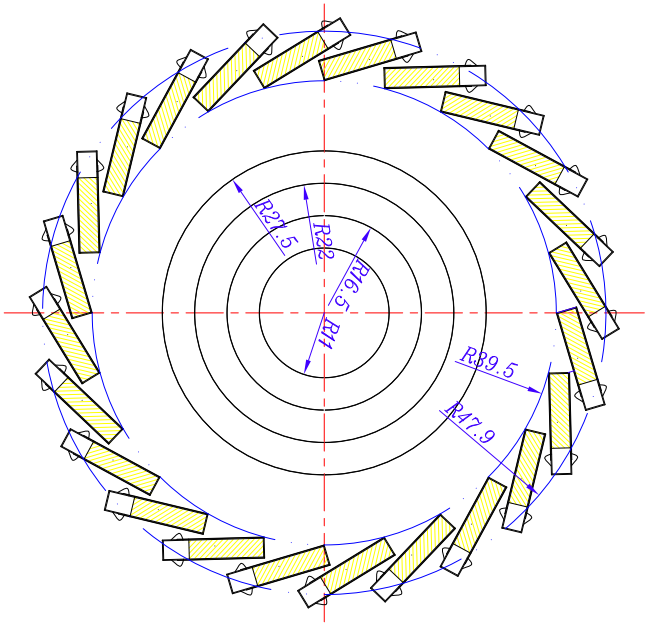

Figure 4.2: Sectional view of the VTX layout. The inner four layers are bent MAPS with semicircular structure and for the 5th and 6th layers are double-layer planar CMOS sensors with ladder desgin.

Table 4.3: Geometric configuration parameters. Radius and length, and material budget of the support structure for each layer of the VTX, as well as the arc length corresponding to Curved Vertex Layer (CVTX) and the height of ladder corresponding to Planar Vertex Layer (PVTX).

CVTX/ PVTX X	radius mm	length mm	arc length mm	height mm	support thickness μm
CVTX 1	11.1	161.4	69.1	-	45
CVTX 2	16.6	242.2	103.7	-	32
CVTX 3	22.1	323.0	138.2	-	31
CVTX 4	27.6	403.8	172.8	-	29
PVTX 5-6	39.5	682.0	-	3.3	300

semiconductor manufacturing technology and processes, the sensors are arranged on 300 mm wafers, and the length of a complete sensor is constrained by the wafer size. As a result, the number of sensors used in the z-direction varies for different CVTXs. Based on the radius and length requirements of the CVTX, a 17.277 $\times$ 20.000 mm^2 Repeated Sensor Unit (RSU) is defined as the basic unit (see Section 4.2.2.1). Three stitched sensors of different sizes are designed on a wafer, as shown in the type A/B/C in Figure 4.3. Each type of sensor comprises modules arranged in multiple rows, where a module integrates several RSUs along with I/O pads positioned at both the left and right edges.

CVTX 1 and CVTX 3 share the type C sensor, with CVTX 1 containing the two type C sensor of the 2 modules. CVTX 2 utilizes the type A sensor, consisting of two

Draft v0.3.1

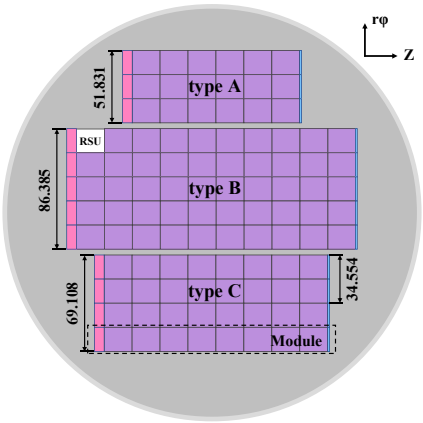

Figure 4.3: The arrangement of stitching frames on a 300 mm wafer. The purple part represents the RSUs, the pink represents the Left-end Readout Block (LRB), and the blue represents the Right-end Power Block (RPB). The short-dashed line area represents a module consisting of several RSUs, one LRB, and one RPB. To meet the requirements of each layer of the vertex detector, the type A/B/C sensors are designed with different lengths and widths. The type A and B sensors are used to make one of the sensors for CVTX 2 and CVTX 4, respectively. The full type C sensor can be used for one of the sensors for CVTX 3. The type C sensor can be divided into four modules along the vertical direction. Using two modules of the type C sensor can make a sensor for CVTX 1.

type A sensor 3 modules arranged along the z-direction and two type A sensor 3 modules arranged along ϕ-direction. CVTX 3 employs the type C sensor, consisting of two type C sensor 4 modules arranged along the z-direction and two type C sensor 4 modules arranged along the ϕ-direction. CVTX 4 adopts the type B sensor, consisting of two type B sensor 5 modules arranged along the z-direction and two type B sensor 5 modules arranged along the ϕ-direction. CVTXs 2, 3, and 4 are spliced in the z-direction, resulting in a 0.5 mm splicing seam at $z = 0$.

Considering the mechanical dead zones in the ϕ direction and the dead zones in the width of the whole sensor, the CVTX 1, CVTX 2, CVTX 3, and CVTX 4 of the vertex detector are rotated by an angle when mounted. This angular adjustment minimizes the occurrence of multiple dead zones at the same angle in the $r\phi$ plane. Each semicircular structure is supported by a material with a specific thickness (see Section 4.3.1.4).

Double-sided Ladders The fifth and sixth layers are constructed using Taichu chips, each sized 15.9 $\times$ 25.7 mm^2 with a thickness of 40 μm. The back of the chip is guled to the Flexible Printed Circuit (FPC) that conducts power and transmits the signal. The chip is treated as a unit, and the dead zones of the adhesive are arranged from the $-z/2$ region to the $z/2$ region at intervals of 0.1 mm. The FPC is glued to both sides of the support structure Carbon Fiber Reinforced Polymer (CFRP) to create a complete ladder cell as shown in Figure 4.4, where the effective thickness of the support structure CFRP hollow pipe is 300 μm, as described in the Section 4.3.1.3. The geometric center of the

Draft v0.3.1

ladder unit rotates around the origin at a specific radius position from the $\phi = 0$ position, while maintaining the height of the wire, forming a barrel structure known as PVTX 5-6 to ensure that no particles leak out in the ϕ-direction. A total of 24 ladder structures are utilized in the fifth and sixth layers.

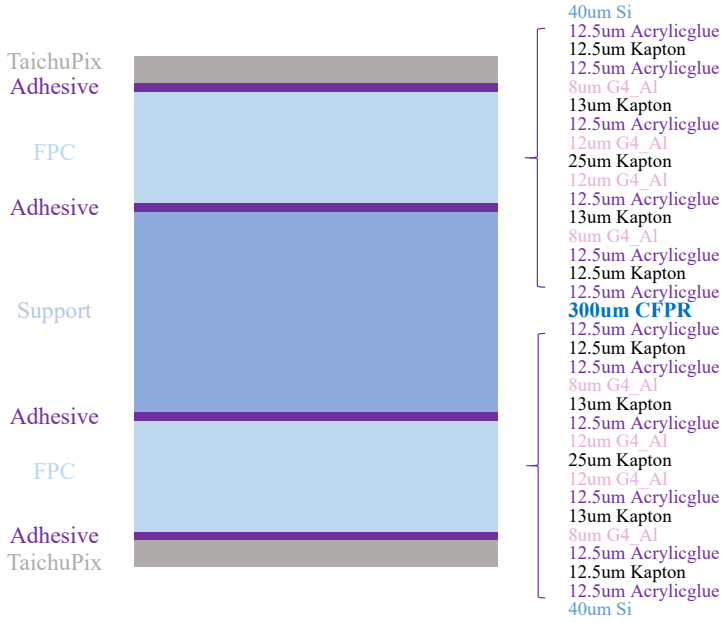

Figure 4.4: Longitudinal cross-section of a ladder, composed of two layers of chips and other materials, such as glue, carbon fiber, and aluminum. Each ladder of PVTX 5-6 in the vertex layout utilizes this structure.

Material budget Figure 4.5 shows the variation of the average material budget X_0 with θ in the ϕ-direction. Table 4.4 lists the material budget of each layer for the VTX at θ = 90°.

Table 4.4: The material budget parameters of each layer for the vertex detector.

Unit	Beampipe	layer 1	layer 2	layer 3	layer 4	layer 5	layer 6
$\bar{X_0}$ (%X_0)	0.454	0.067	0.059	0.058	0.061	0.280	0.280

4.1.3 Background estimation

As a kind of important information, the hit rate significantly affects the design specifications of the sensor. The details of each component's contribution to the VTX will be discussed in the Chapter **??**. In this subsection, we will only present the total hit rate, data rate, occupancy, and other relevant information for each mode. With hit rate being defined as the frequency of particles hitting the RSU, data rate equals to hit rate times

Draft v0.3.1

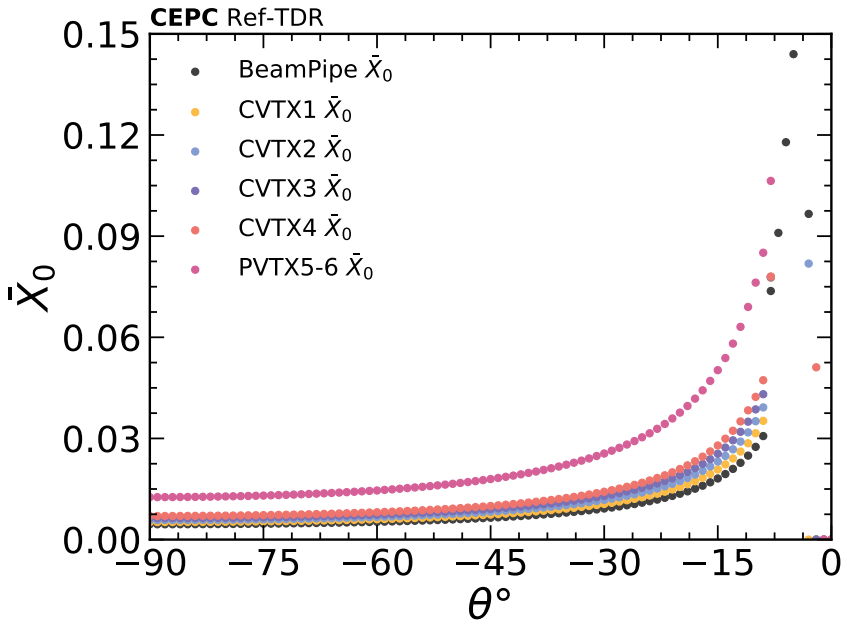

Figure 4.5: The average value $\bar{X}_0$ within the range of $\phi \in (0, 360)°$ of vertex detector varies with θ.

cluster size, which indicates the number of pixels fired by a single particle, and occupancy is calculated within a specified time window at pixel level.

In order to calculate the data rate, information about the cluster size is essential. To compute the data rate more accurately, we did not set the cluster size as a fixed value; instead, we referenced the results from the TaichuPix-3 beam test and calculated the cluster size based on the particle's incidence angle. The background hit rate and data rate are shown as Table 4.5, and the hit rate distributions of Higgs as well as Z mode are shown as Figure 4.6 and Figure 4.7.

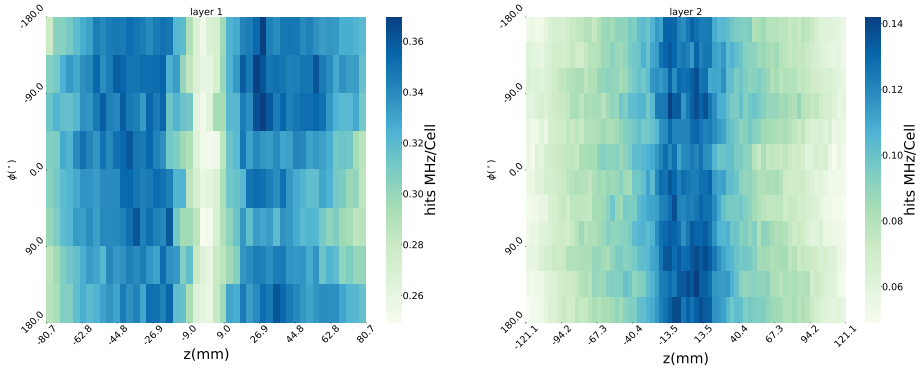

Figure 4.6: Hit rate distribution of Higgs mode. The shape of VTX is approximately cylindrical, where the x-axis can be equivalently regarded as the z-axis of the global coordinate, and the y-axis can be equivalently regarded as the polar angle ϕ of the global coordinate. Synchrotron radiation is not included.

Draft v0.3.1

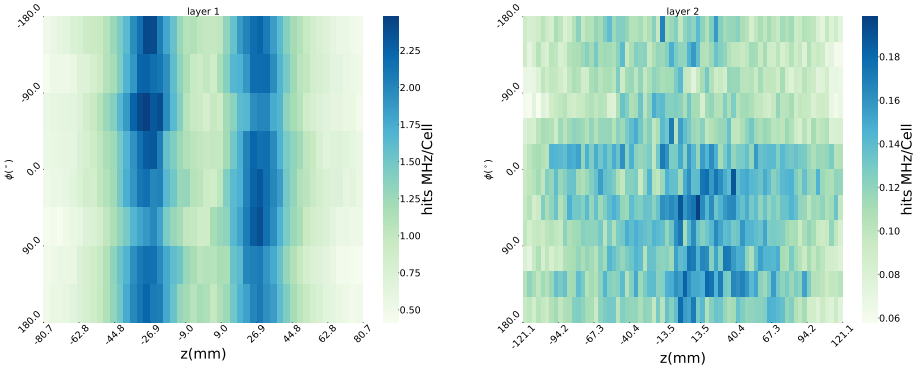

Figure 4.7: Hit rate distribution of Z mode. For we could not completely handle high-lumi Z mode now, as well as the major difference between high-lumi Z with Z mode is luminosity which means their hit rate distribution is similar, the hit rate distribution of high-lumi Z would not be shown here. Synchrotron radiation is not included.

Table 4.5: Summary of background estimation. Current detector scheme cannot completely handle high-lumi Z mode, so the result of high-lumi Z will not be shown here. For the results of high-lumi Z, based on accelerator parameters, a rough estimation can be made by simply multiplying the existing Z mode results by a factor of 3. Synchrotron radiation is included.

Layer	**Ave. Hit Rate MHz/cm^2**	**Max. Hit Rate MHz/cm^2**	**Ave. Hit Rate×C MHz/cm^2**	**Max. Hit Rate×C MHz/cm^2**	**Ave. Data Rate Mbps/cm^2**	**Max. Data Rate Mbps/cm^2**
Higgs: DataRate = HitRate ×32 bit / pixel × ClusterSize @(Bunch Spacing: 277ns, 63 %Gap, 25× 25 μm^2/ pixel)						
1	2.5	2.8	8.2	10	260	340
2	0.67	1.1	2.2	3.5	70	110
3	0.17	0.35	0.62	1.2	20	38
4	0.078	0.18	0.32	0.98	10	31
5	0.026	0.15	0.11	0.74	3.4	24
6	0.018	0.085	0.074	0.41	2.4	13
Z mode: DataRate = HitRate ×32 bit / pixel × ClusterSize @(Bunch Spacing: 69ns, 9 %Gap, 25× 25 μm^2/ pixel)						
1	9.4	19	42	88	1400	2800
2	0.89	1.5	3.7	7.5	120	240
3	0.31	0.75	1.5	6.0	46	190
4	0.19	0.47	0.95	4.9	30	160
5	0.045	0.095	0.20	0.45	6.4	14
6	0.035	0.072	0.15	0.38	4.8	12

For the VTX, the primary sources of beam background are synchrotron radiation and pair production. However, due to the excessive computational resources required for simulating and analyzing synchrotron radiation, we did not perform simulations and analyses with the same event statistics and granularity as those for other beam backgrounds. Based on simulation results of approximately 1×10^9 synchrotron photons, we estimate that the beam background contribution from synchrotron radiation is comparable to that from pair production. Therefore, when presenting Table 4.5, to incorporate the synchrotron radiation results, we multiplied the pair production contribution by a factor of 2. However,

Draft v0.3.1

it should be noted that the actual maximum value will be lower than simply doubling the pair production results.

We used a bunch spacing as a time window to calculate the occupancy of different modes at various levels, and the results are as Table 4.6.

Table 4.6: Occupancy estimation. Considering that the only difference between the two modes in the current simulation lies in the bunch settings, the occupancy in both modes should be similar. Therefore, they are combined and presented as Z mode. Synchrotron radiation is not included.

Layer	Mode	Ave. Occupancy@Pixel ($\times 10^{-5}$ / BX)	Max. Occupancy@Pixel ($\times 10^{-5}$ / BX)
1	Higgs	1.818	2.331
2		0.484	0.778
3		0.137	0.265
4		0.071	0.219
5		0.024	0.170
6		0.017	0.095
1	Z Mode	0.972	2.026
2		0.085	0.168
3		0.033	0.124
4		0.022	0.108
5		0.005	0.011
6		0.004	0.009

4.2 Sensors and electronics design

4.2.1 Sensor technology overview

The current design and development of the CEPC vertex detector are centered on utilizing MAPS technology for chip design and manufacturing. This technology integrates the sensor and readout electronics onto a single chip, significantly reducing both pixel size and power consumption while delivering high-performance detection capabilities. Such features meet the stringent requirements for high resolution, low material budget, and rapid readout speeds.

The Solenoidal Tracker at RHIC (STAR) experiment at Relativistic Heavy Ion Collider (RHIC) successfully employs MAPS technology in its vertex detector [1], and the STAR MAPS vertex detector features excellent spatial resolution [1, 2]. The Inner Tracker System (ITS)2 of European Organization for Nuclear Research (CERN)'s A Large Ion Collider Experiment (ALICE) experiment is the largest scale MAPS system among high energy physics experiments [3]. ITS2 is a full-pixel silicon detector based on TowerJazz 180 nm technology. It boasts exceptional technical parameters, including approximately 5 μm high resolution, an extremely low material budget of less than 0.3 % X_0 per layer, stable readout support for collision frequencies up to 100 kHz, and power consumption as

Draft v0.3.1

low as 40 mW·cm^{-2} [3, 4]. The upcoming ITS3 upgrade for the ALICE experiment introduces the concept of "curved wafer-level chips", aiming to achieve a self-supporting wafer structure [5, 6]. This development is based on TowerJazz Tower Partners Semiconductor Co. (TPSCo) 65 nm technology. This innovation could potentially reduce the material budget of the vertex detector by a factor of 3 to 5. The ITS3 project is currently in the research and development phase. The comparison of key parameters between different vertex detectors mentioned above is shown as Teble 4.7.

Table 4.7: Comparison of sensor technology in vertex detectors of different experiments: ALICE Pixel Detector (ALPIDE)(ALICE ITS2), MOSAIX(ALICE ITS3), Taichu-3 (the first CEPC vertex detector prototype), and Taichu-Stitching(CEPC vertex detector).

Sensors	Technology Node	Power Consumption	Readout Speed	Spatial Resolution
ALPIDE [3, 4]	180 nm	$40\text{mW}/\text{cm}^2$	Up to 100 kHz	5 μm
MOSAIX [5]	65 nm	$40\text{mW}/\text{cm}^2$	164 kHz	5 μm
Taichu-3 [7–9]	180 nm	$80 \sim 100\text{mW}/\text{cm}^2$	40 MHz	5 μm
Taichu-Stitching	65 nm	$\leq 40\text{mW}/\text{cm}^2$	Up to 43 MHz	3-5 μm

4.2.2 Stitched sensor prototype design

The stitching technology enables the production of chips significantly larger than the dimensions of the design reticle. The design reticle is divided into sub-frames that align with the sub-frames of the photomasks. By selectively exposing these reticle sub-frames onto adjacent locations following the designed pattern, manufacturers can create large chips with dimensions nearing the wafer's diameter. This innovative approach expands the possibilities for chip design and production, allowing for more efficient utilization of wafer space. This technology is particularly advantageous for pixel sensor chips that feature a high number of repeated units (pixel matrices) and demand a large active area. Taking into account the difficulty and the yield of stitching technology, the baseline design of the stitched sensor prototype involves using 1D stitching to achieve stitched-chip along the beam pipe direction. The feasibility of 2D stitching will also be continuously explored during research and development.

4.2.2.1 Sensor architecture and functional blocks

The idea of using a stitched sensor chip to construct half of the detector layer is inspired by the design of the ALICE ITS3[5][6] sensor. Thanks to the promising results obtained in the MOnolithic Stitched Sensor (MOSS) and MOnolithic Stitched sensor with Timing (MOST) prototypes for the ALICE ITS3 project, this consideration benefits from the scheme of the MOSS and MOST prototype. Detailed R&D on the stitching floor-plan for the vertex detector is under assessment at the time of writing. The preliminary stitching plan of the silicon wafer and the dimensions of each half layer are introduced in Figure 4.3.

Draft v0.3.1

Figure 4.8 presents a schematic floor-plan of the sensor for Layer 1, implemented by dicing out two adjacent modules (the dicing scheme is depicted in Figure 4.3). Each module operates independently. The sensitive area of a module consists of eight RSUs, each representing an instance of the same design. On the left side of the module, the Left-end Readout Block (LRB) facilitates signal interconnections to the external systems and the power supplies to the module. The Right-end Power Block (RPB), located on the right side, consists solely of power transmission buses for the power distribution.

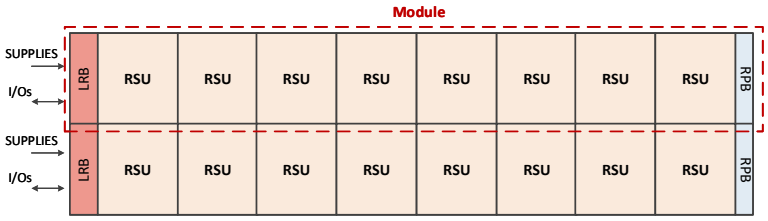

Figure 4.8: Top level floor-plan for a sensor of layer1 (not to scale). It comprises two identical modules, with one of them indicated by the dotted red rectangle.

Figure 4.9 illustrates the preliminary floor-plan of one RSU. One RSU is divided into several identical Sensor Blocks. Each sensor block is fully independent from the others with its own biasing generator, slow control and periphery readout circuit, shown in Figure 4.10. The sensor block has local power switches located at the right side of the sensor block that can be selectively switched on by the user control. This powering granularity reduces the sensitivity of the stitched sensor to possible manufacturing faults. In the case of a supply short in one of the sensor blocks, it allows to switch off the faulty sensor blocks and maintain the others functioning normally. Considering the sensitive area of a sensor block will introduce an extra dead area in the event of switching off, the dimension of the pixel matrix in a sensor block should be choose carefully. The scale of a sensor block will be optimized in the future design for a trade-off between the power granularity and the data transmission performance. In the preliminary design at the time of writing, one RSU contains 12 identical sensor blocks and 4 stitched interface blocks arranged in two rows. Data of each sensor block has to be transmitted to the LRB through the one-to-one direct connection between the sensor block and the LRB. As the longest transmission distance reaches more than 20 cm for the rightmost sensor block of the module, the regeneration of the signal periodically over the link is necessary. This function is proposed to be implemented in the stitched data interface blocks. The stitched data interface block transmits control signals and data from sensor blocks to the LRB. As the RSU is divided into multiple sections internally, different functional blocks are repeated multiple times. An RSU contains 12 Pixel Matrices, Biasing Blocks, Power Switches Blocks, and Matrix Readout Blocks, and 4 Stitched Data interface Blocks.

Draft v0.3.1

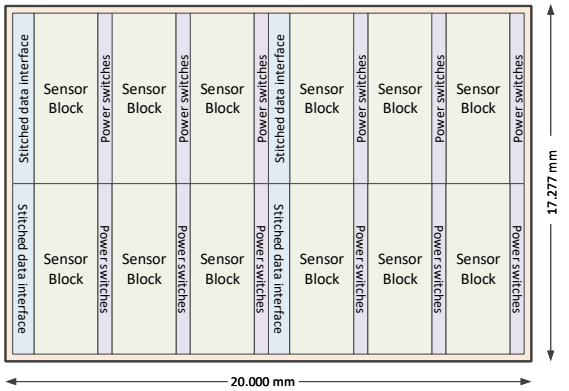

Figure 4.9: Proposed floor-plan for a RSU (not to scale). It contains several identical sensor blocks. Each of them has a pixel matrix with its own biasing generator, slow control and periphery readout circuit. Each sensor block can be selectively switched on/off. The stitched data interface blocks are used to transmit control signals and data to the edge of the stitching sensor.

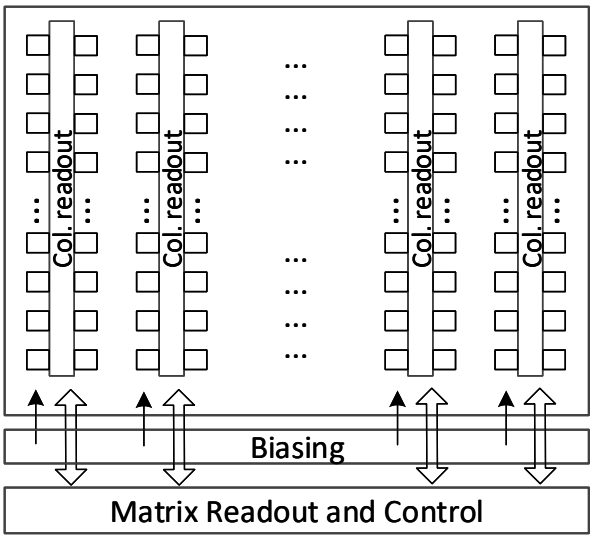

Figure 4.10: Architecture of the sensor block. It consists of a pixel matrix, a biasing generator and a periphery readout and control.

4.2.2.2 Design of the repeated sensor unit

Each pixel cell integrates a sensing diode, a front-end amplifier, a discriminator and a digital pixel readout. The in-pixel digital readout benefited from the TaichuPix prototype. Each pixel contains a hit storage register and logic for pixel mask and test pulse configuration. A common threshold level is applied to all the discriminators of the pixels. Every pixel can be tested and calibrated individually, combining charge injection scans and threshold scans.

Draft v0.3.1

I. Sensing diode As depicted in Figure 4.11, the collection N-well electrode has an octagonal shape fabricated on a P-type epitaxial layer. The collection electrode is surrounded by the P-guard ring. The space between the collecting N-well and the surrounding P-well is introduced to increase the depletion region and thus enhance the charge collection efficiency. Footprint represents the total area defined by the surrounding P-well. The design of the sensing diode geometry is a compromise among the charge collection performance (i.e. charge collection efficiency and time, radiation tolerance), area, and sensor capacitance. As mentioned in Section 4.5.1, the optimization of sensor performance was previously addressed in the 180 nm TowerJazz CMOS technology. These studies offer valuable insights for enhancing sensor performance in the 65 nm TowerJazz CMOS technology. To further optimize the sensor geometry to align with the 65 nm CMOS process, pixel test structures are proposed to be designed in the initial phase of the stitched sensor R&D. Various sensor variants in the test structures encompass different electrode diameters, spacing between electrode and surrounding PWELL, PWELL shapes, and the method of applying reverse bias to the sensor diode.

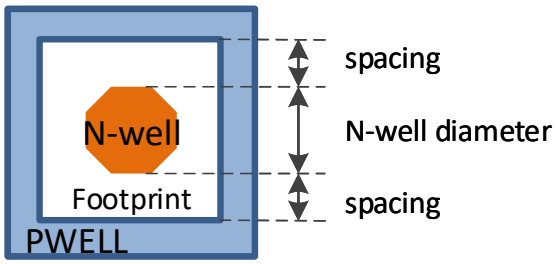

Figure 4.11: Geometry of the sensing diode. It consists of the collecting N-well and the surrounding P-well.

II. Pixel Front-end The simplified schematic of the analogue front-end is shown in Figure 4.12a, which had been verified in the TaichuPix prototype (see Section 4.5.2). The topology of the circuit was derived from the ALPIDE sensor chip used in the ALICE ITS2 [4]. The analog front-end and the discriminator are continuously active.

III. In-pixel digital logic The in-pixel digital electronics inherit the TaichuPix design. Figure 4.12b presents the diagram of the in-pixel logic. It features a hit latch set by a negative pulse from the output of the front-end. The pixel readout follows a double-column drain arrangement. The region for in-pixel digital readout logic is shared by two columns to minimize the crosstalk between analog signals and digital buses. Additionally, it saves space for the routing of the address encoder. The priority logic arbitrates the pixel readout, with the topmost pixel having the highest readout priority. The in-pixel logic also integrates configuration registers for calibrating the pixel front-end, for testing in-pixel readout logic, and for masking the faulty pixel. The configuration function is

Draft v0.3.1

programmable through the setting of control bits, including MASK_EN, PULSE_EN, DPULSE and APULSE (as shown in Figure 4.12b).

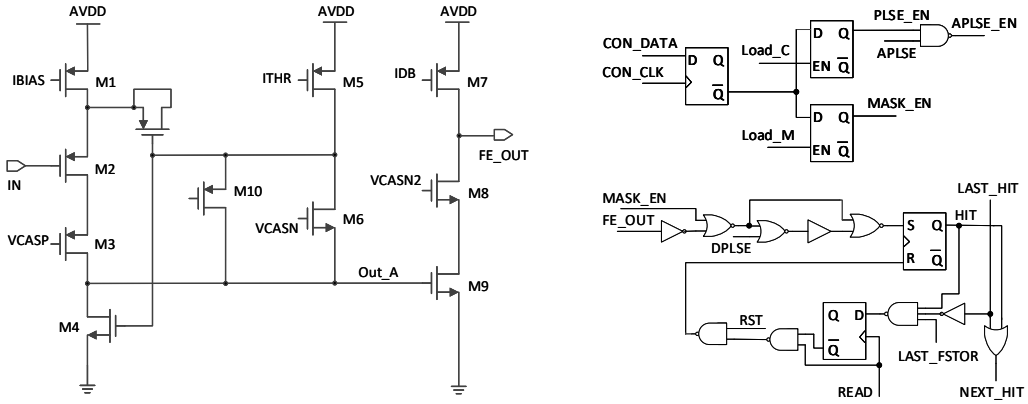

(a) Schematic of the analog front-end. **(b)** Diagram of the digital logic.

Figure 4.12: Schematic and block diagram of the in-pixel circuits.

IV. Peripheral readout circuits on sensor The main function of the on-chip peripheral readout circuits includes: sending the control signals required by the pixel array and receiving the data from the pixel array; buffering the data to smooth the output data rate; providing a slow control interface for chip configurations and tests.

The data from the pixel array are organized in Double Columns (Dcols). In order to achieve a detection efficiency close to 100 %, all double columns of pixel array are read out in parallel. A timestamp is recorded at the end of the double column for the future data processing. Without a trigger signal, all the readout data are buffered and output. A data compression mode is optional, which will reduce the output data rate by half.

The peripheral readout circuit's core function is to send control signals to the pixel array and receive data from it. A data-driven schema is preferred. The read signal is only sent when the pixel is triggered. To read the signals sequentially, a priority mechanism must be implemented. The most popular method is address priority. A hit signal is generated when the collected signal exceeds a threshold and is reset after the pixel address is read out.

Based on this approach, the pixel array's clock is inactive in the absence of a hit. This approach effectively minimizes power consumption. To optimize control timing, a hierarchical priority control chain can be implemented.

To accommodate higher data rates, a real-time data compression strategy can be implemented before sending data to First In First Out (FIFO)s.

The address of the first pixel in a package is recorded, while the next three pixels are encoded using a three-bit code, where '0' represents no hit and '1' represents a hit. Operating at a system clock of 43.33 MHz, the data compression circuits incur no

Draft v0.3.1

additional timing overhead. By enabling the data compression function, the data volume is reduced, and the readout speed is increased.

The fast chip-level readout is closely related to FIFO accesses. We propose a shareable architecture [10]. The shared FIFO features flexible capacities to handle random hit bursts. As a result, higher hit flux can be accommodated even with a reduced total memory volume.

The power consumption is evaluated based on TaichuPix, which is implemented using a 180 nm process for average hit rates of 1 MPixels/s·cm^2, 15 MPixels/s·cm^2, and 40 MPixels/s·cm^2. The future design of the RSU will use a 65 nm process. The power supply will be reduced from 1.8 V to 1.2 V. The area of the peripheral readout circuits is estimated to be reduced by 50 %. The dynamic power consumption due to clock and data upsets is estimated with a reduction of 4.5 times. However, the static leakage currents will increase significantly. To meet the power density of 40 mW/cm^2, the power consumption of peripheral circuits in RSU is estimated to be 40 mW, the leakage current should be controlled in 5 times of TaichuPix. Power switches will be implemented to meet these requirements. Finally, the power consumption of the future design is estimated as 29 mW and 37.5 mW for 8 MPixels/(s·cm^2) at Higgs mode and 42 MPixels/(s·cm^2) at Z mode, respectively.

Considering the application and tests, the sensor chip will provide proper register control and on-chip test mode.The On-Chip Test (OCT) module is planned to generate input signals for peripheral readout circuits, enable chip debug and data alignment. The register control provides internal status access and configuration of readout function, bias voltage/current, pixel mask and calibration, and so on.

4.2.2.3 Design of the left-end readout block

All data from the RSUs per module (see Figure 4.8) are collected and processed by the LRB located on the left side of each module. The block diagram of Figure 4.13 illustrates the primary functions of the LRB. The RSU data are transmitted to the LRB via a large array of differential point-to-point on-chip serial data links, which operate at 86.66 Mbps. As noted in Section 4.1.2, individual modules from different layers in the detector contain varying numbers of RSUs, with the module in Layer 4 housing the largest quantity, i.e. 10 RSUs. Since each RSU is equipped with 12 data links, the LRB must accommodate up to 120 data links. A group of 128 receivers primarily compensates for phase differences in the incoming data streams from the RSUs and resamples them using a local fast clock. The data encoding blocks collect and encode the data with redundancy to correct errors during off-chip transmission. After encoding, the data are serialized at a rate of 1.39 Gbps and transmitted off-chip using 8 serializers. The Clock Block supplies the clocks required for the LRB and RSUs. Additionally, the LRB facilitates slow control and manages power switch control signals for the RSUs.

Draft v0.3.1

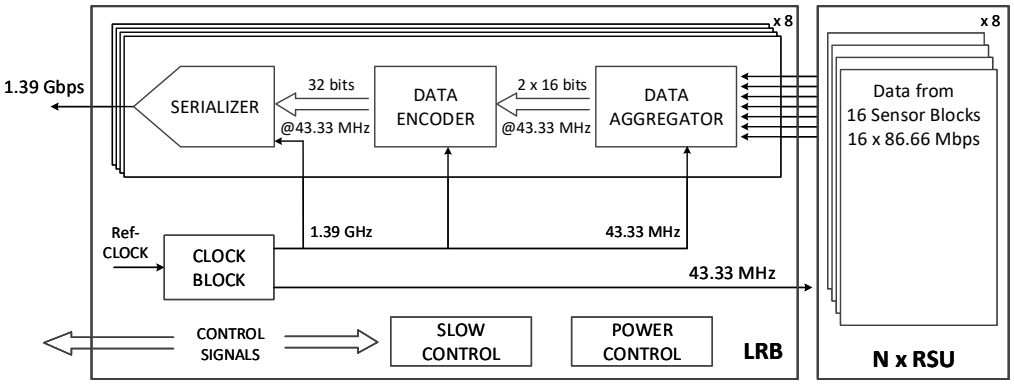

Figure 4.13: Proposed diagram of the LRB. All data from RSUs of one module has to be transmitted to the LRB. 'N $\times$ RSU' labeled in the right part of the diagram represents that different layers in the detector contain a varying number of RSUs.

4.2.2.4 Power consumption estimates

As illustrated in Figure 4.9 and 4.10, each RSU consists of pixel matrix, biasing blocks, matrix readouts, and data interface blocks. Table 4.8 provides the expected power consumption of the main functional blocks of the RSU and the total power consumption of a single RSU. The current consumption is mainly determined by the bias current (IBIAS) of the first branch, adjustable by one of the local Digital-to-Analog Converter (DAC)s in the periphery of the pixel array. Targeting the power requirement of 40 mW/cm^2, the value of IBIAS is reduced compared to the one in the TaichuPix design. The choice of the IBIAS value is a trade-off between the power consumption and the speed. By design, the nominal power consumption values of the new front-end in TPSCo 65 nm process are 68.4 nW. The nominal value corresponds to analogue power densities of 26.7 mW/cm^2 for the pixel pitch of 16 μm and 10.9 mW/cm^2 for the pixel pitch of 25 μm. In Table 4.8, the entries for the pixel matrix include the power of the pixel analogue circuit and the pixel digital logic. In the current calculations, it is assumed that the pixel size is 25 $\times$ 25 μm^2, which is consistent with the intrinsic position resolution value used in Section 4.1.2. The power of the pixel analogue is calculated by the power density of the pixel front-end (shown in Section 4.2.2.2) and the total area of 12 pixel matrices. The power consumption of the pixel digital in the table includes the dynamic power of the in-pixel digital logic and the double-column address encoding logic (described in Section 4.2.2.2), as well as power consumption due to the leakage current. The dynamic power consumption of the pixel digital circuit mainly depends on the pixel hit rate. Based on estimations of the hit rate in the vertex detector and testing experience with the TaichuPix prototype, the dynamic power consumption of the pixel digital circuit is relatively small. In contrast, considering the planned use of 65 nm CMOS process, the contribution of leakage current from transistor gate leakage to power consumption is much greater than the dynamic power of the digital circuit. The contribution of the Biasing Blocks is estimated based on

Draft v0.3.1

the experience of the design in the TaichuPix. The entry for the Matrix readout blocks is described in Section 4.2.2.2. The value for the data interface blocks is obtained from the very preliminary considerations on the transmitting power of the control signals and the readout data of RSUs. Table 4.9 lists the power consumption estimates for the main functional blocks of the LRB (see Figure 4.13).

Table 4.8: Estimates of power consumption of one RSU. All values are for 27 °C temperature and 1.2 V power supply voltage.

Components	Pixel analogue	Pixel digital	Biasing block	Matrix readout	Data interface	RSU Total
Power [mW]	36	30	8	40	17	131

Table 4.9: Estimates of power consumption of the LRB. All values are for 27 °C temperature and 1.2 V power supply voltage.

Components	Clock Block	Data Aggregator	Data Encoder	Serializer	Slow & Power control	LRBTotal
Power [mW]	36	120	80	32	80	348

Combining the power estimates of Table 4.8 and 4.9 with the surface areas of the major blocks, one obtains the estimates for the power dissipation densities. The results are given in Table 4.10.

Table 4.10: Estimates of average power dissipation per unit area over the main functional blocks composing the stitched chip

Components	Power density [mW/cm^2]
Repeated Sensor Unit	38
Left-end Readout Block	485

4.2.3 Backend electronics and cables

In the vertex detector design, flex Printed Circuit Board (PCB)s are integral to the backend electronics system. These flex PCBs serve as conduits for transmitting signals, clocks, control commands, power, and ground connections between the control boards and the detector modules. By providing a lightweight and adaptable interconnection, flex PCBs facilitate efficient data communication and power distribution while minimizing material usage, which is crucial for maintaining the detector's performance and reducing multiple scattering effects.

Draft v0.3.1

4.3 Mechanics, cooling and services

This section describes the mechanical design of the VTX, including the support structure and related finite element analysis, detector air cooling and the general scheme of services.

4.3.1 Mechanics

4.3.1.1 General support structure

The baseline design of the vertex detector consists of, from inner radius to outer radius, four concentric cylinders constructed with stitching technology-based bent MAPS followed by a single-layer double-sided ladder-based barrel. The innermost cylinder has a radius of 11 mm, and maintains a 0.3 mm gap from the beam pipe. As shown in Figure 4.1, the side view along the beam direction, this figure demonstrates the general structure of the detector and its integrated mechanical support. To be consistent with the physics requirements and goals, the general mechanical support design for the Vertex detector aims to use ultra-light materials to create a rigid enough structure, realizing a low material budget without weakening the spatial resolution.

4.3.1.2 Ladder and support

The double-sided ladder is the structural unit of the layer 5 and 6 . It features pixel sensors on both sides of the ladder support, while sensors are glued onto the FPC, which is also glued onto the ladder support. The CFRP is used to make the ladder support due to its low density and high specific modulus and strength. The main body of the ladder support [11] is a hollow shell structure [11] with an overall size of $682 \times 3.2 \times 17.5$ mm^3 . With the assistance of the finite element static analysis, the laminated shell of the ladder support is made of ultra-thin CFRP plies, using the high modulus CFRP at a level equivalent to M40, the CFRP laminate of the shell is made with a thickness of 0.15 mm, to get a conservative estimation by just putting the mass of the sensors and FPC to the bare ladder support (without taking into account their contribution to the rigidity of the complete ladder), it is anticipated that the ladder support deforms very slightly and at a negligible level. According to previous evaluations, about 20 % smaller deformation will be induced for the complete ladder [11].

4.3.1.3 Ladder-based barrel and fixation to the beam pipe (assembly)

The vertex detector is the first detector outside the beam pipe, and structurally it will be integrated into the beam pipe assembly. The outer most layer of the vertex detector, the ladder-based barrel, does not directly mount on the beam pipe; it rests and is secured to

Draft v0.3.1

the intermediate conical parts that are mounted to the beam pipe, providing support for the vertex structure. The four layers of bent MAPS cylinders are mainly fixed to the extended section of the beam pipe.

The barrel-shaped outer layer detector formed by the double-sided ladders which overlap with each other in the circumferential direction to form a continuous sensitive layer. To facilitate barrel assembling and its installation on the beam pipe integration, the barrel structure is designed as Figure 4.14 shows , it is assembled by two half-barrels, each half-barrel consisting of two half side-rings located at both ends along with several ladders. The ladders are positioned and secured to the side-rings by the surfaces of the tooth-shaped structure of the side-rings. After the two independent half-barrels are pre-assembled on dedicated tooling, they are installed and fixed onto the intermediate conical part of the beam pipe assembly , as illustrated by Figure 4.14 .

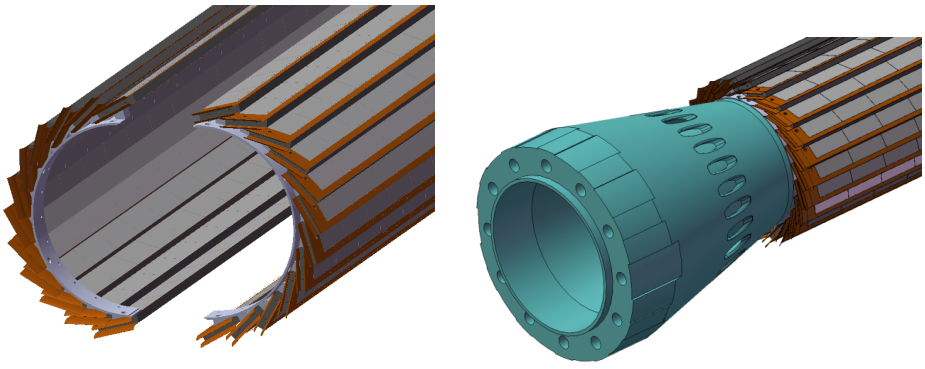

(a) **(b)**

Figure 4.14: (a) The barrel assembly. (b) The barrel on beam pipe assembly (the outer tube of the beam pipe assembly is not shown)

Structurally, the ladder-based barrel design is consistent with our previous prototyped vertex design. Furthermore, much R&D work involving structural validation tests were conducted during the previous prototype development phase, these experiences can be helpful to optimize the TDR design.

4.3.1.4 Bent MAPS cylinders and fixation to beam pipe

There are four layers of bent MAPS cylinders with different radii and lengths consistent with the physical layout of the vertex detector. Each of the four bent MAPS cylinders is a single detector layer that consists of two half cylinders, as shown in Figure 4.15. To maintain the bent MAPS in the shape of the cylinders, ultra-light local supports made of CFRP have been designed for each layer. Integrated with the electronic readout, the FPC is connected to the curved edge of the bent MAPS on its lateral side by wire bonding . To keep the connecting joint safe and also for protecting the wire bonds, extended support

Draft v0.3.1

has been designed for each cylinder, as shown in Figure 4.15, it prevents the FPC from deforming very close to the joint area, thereby avoiding damage to the connection. The bent MAPSs, the local support and the extended support form the cylinder assembly. Each cylinder assembly is independent and has no contact with the adjacent layers of cylinder assemblies, also will be mounted onto the beam pipe assembly separately . This kind of design focuses primarily on realizing and facilitating a feasible process for both assembly and wire bonding, as well as installation onto the beam pipe. The results of the finite element simulation analysis indicate that, under constrained conditions at both ends, this structure has very minimal deformation, and the stress on the bent chips is also very low, both of which are negligible, taking the innermost layer bent MAPS cylinder assembly as an example. In addition, some R&D studies of making the bent MAPS have been done; so far, the dummy wafer with a thickness of 40 μm and a radius of 12 mm has been tested and proven to be feasible, refer to Section 4.5.2.3.

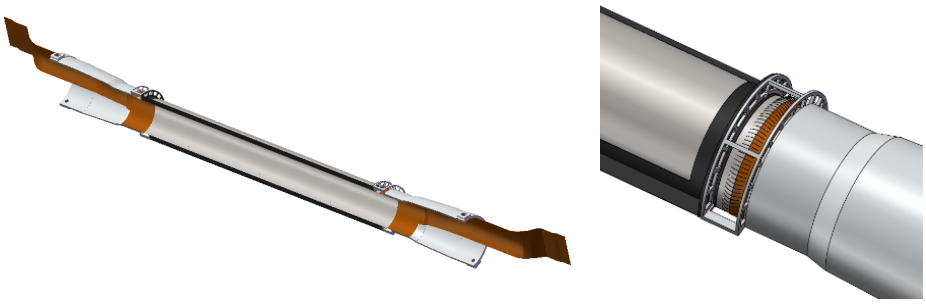

(a) **(b)**

Figure 4.15: The half cylinder assembly (bent MAPS with FPC and the extended support) of the innermost layer. (a) An overview of the half cylinder of bent MAPS detector layer, and the yellow part is FPC. (b) An extended support to prevent the FPC from deforming too close to the joint area.

4.3.2 Cooling

The heat generation of the Vertex detector for both the ladder-based barrel and the bent MAPS cylinders is estimated to be at the same level of 40 mW/cm^2. The operational temperature for the detector is required to be no higher than 30 °C. Thus, cooling is essential for maintaining optimal sensor performance. Generally, electronic equipment with heat generation up to 0.3 W/cm^2 can be cooled using forced air convection. Given the stringent material budget requirements for the vertex detector, compressed air cooling has been selected as the cooling method.

To evaluate the cooling performance of the current structural design of the vertex detector , air cooling simulation analysis was conducted. The simulation results indicated that at an average flow rate of 3.5 m/s, the maximum temperature of the outer ladder is

Draft v0.3.1

Table 4.11: Simulation results of the barrel-maximum temperature on the ladder. Inlet air temperature of 5 °C; air speed of 3.5 m/s.

Power dissipation	Total heat generation of the barrel	Max temperature on ladder
40 mW/cm^2	190 W	29.4 °C

within the required range, as shown in Table 4.11. For the bent MAPS cylinders, the innermost layer is very close to the beam pipe and has no airflow, making it the most challenging layer to cool within the entire detector. The simulation results indicate that at an airflow rate of 3.5 m/s (which satisfies the ladder cooling), with the central beam pipe surface temperature considered, the innermost layer of the bent MAPS cylinder can be cooled to a sufficiently low temperature, as shown in Figure 4.16, thereby meeting the experimental requirements. Additionally, simulations were performed to compare the maximum temperature of the innermost layer at different wind speeds. Based on these simulation results, it can be anticipated that air cooling will meet the current cooling needs of the detector.

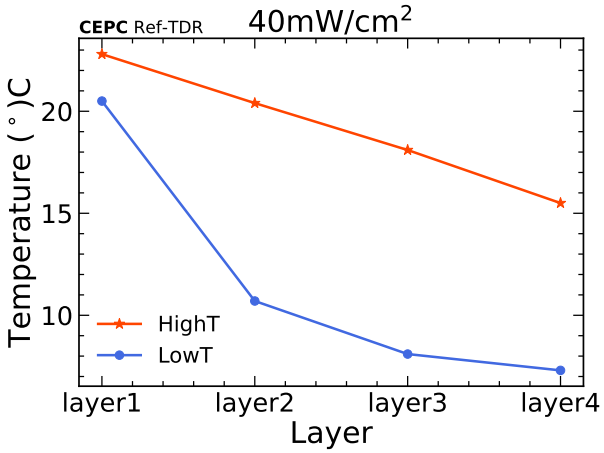

Figure 4.16: Simulation results for the cooling of bent MAPS cylinders, with an airflow rate of 3.5 m/s. The beam pipe surface temperature, as shown in Chapter **??**, is taken into account.

4.3.3 Services

This section introduces the needs and considerations of the general services for the Vertex detector. The vertex uses air cooling; the main service requirement is to ensure proper airflow and good ventilation for the entire detector zone. The vertex detector will be mounted onto and integrated into the beam pipe assembly; the other service requirement is to route all the cables of the VTX out of the very space-limited beam pipe assembly.

Since the VTX consists of a single barrel layer and four concentric cylinder layers, ventilation for each gap between the adjacent layers must be ensured for effective cooling.

Draft v0.3.1

The mechanical design for the vertex detector fully considered this requirement and also tried to minimize the effect caused by FPCs blocking, which is obviously reflected in the hollow support structures designed for the detector, especially the support of the bent MAPS cylinders. The conical part that is integrated into the beam pipe assembly to support the barrel layer mentioned before also works as the general air distributor for the entire vertex detector. It is a hollow structure; air will be blown into the inside hollow space from the side of the part then distributed to the detector zone through those ventilation holes facing different zones of the detector on the outer surface, as shown in Figure 4.17.

The space for the entire VTX outside the beam pipe is very compact. Together with the beam pipe assembly, for the vertex detector, on both ends of the barrel and the bent MAPS cylinders, the FPCs of the ladders and the bent MAPS are the only cables that need to be routed out . The FPCs of the bent MAPS cylinders will be routed along their extended support and converged after the end of the outermost layer, and then they are stacked and go through the intermediate conical part via the grooves. The FPCs of the ladders of layer 5 and 6 will be streamlined by converging the FPCs of two adjacent ladders into one conduit, similar to the FPCs of the bent MAPS, then go through the conical part via their specified grooves, as illustrated in Figure 4.17, which effectively halves the spatial occupancy and preventing the circumferential accumulation of FPCs from fully cover the outer surface of the conical part. After all the FPCs are routed outside the beam pipe assembly, they will be transferred to optical fibers via connectors, as described in Section 4.2. Additionally, a half-dummy model of the vertex structure, incorporating the bent MAPS cylinders and two short ladders, was constructed to test the FPC routing . The trial results demonstrated that the routing scheme is fundamentally feasible.

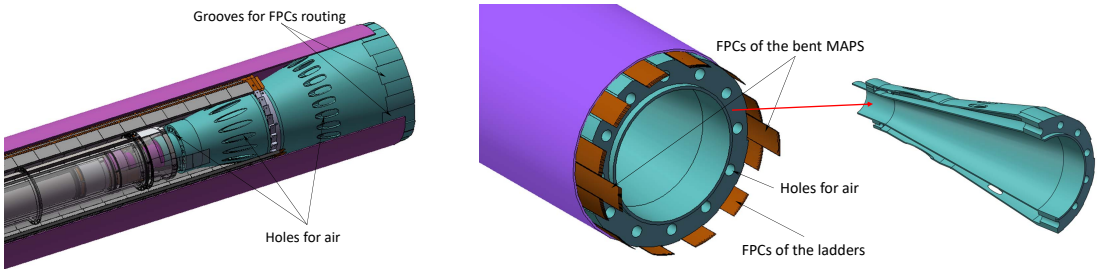

(a) **(b)**

Figure 4.17: Air ventilation and cable routing of the VTX. (a)Air channel design with holes on global support structure for air distribution. Grooves on support structure is designed for FPCs routing. (b) the FPCs of the vertex detector routed out of the side of the beam pipe assembly, along with a cut view of the conical part.

Draft v0.3.1

4.4 Alignment and calibration

The vertex detector is designed to precisely measure the trajectory parameters of charged particles close to the interaction point, enabling accurate reconstruction of decay vertices from short-lived particles. Effective alignment is crucial for achieving optimal resolution in the vertex detector.

The alignment strategy for the vertex detector faces significant challenges due to the implementation of bent wafer-scale monolithic pixel sensors. The primary goals of this strategy include achieving high spatial resolution, reducing uncertainties in impact parameters, and ensuring stable alignment through efficient and automated processes.

4.4.1 Initial mechanical alignment and reference alignment system

Initial mechanical alignment will be conducted during detector assembly, utilizing precision optical survey instruments. Sensors will be aligned within a few micrometers of design specifications, and optical method will confirm sensor curvature and cylindrical positioning. Fiducial markers placed strategically on sensor modules and supporting structures will facilitate optical tracking and ensure precise referencing. A stable external alignment system, regularly monitored through X-ray or laser-based and optical survey methods [12], will serve as the reference for continuous alignment.

4.4.2 Track-based alignment

Mechanical alignment procedures during installation provide an initial level of precision in the vertex detector position. This precision is typically significantly worse than the desired design hit resolution. Additional alignment (tracker-based alignment) is needed to account for the position, orientation, and surface deformations of the MAPS sensors. Charged particle tracks obtained from collision data will facilitate iterative alignment corrections during both the commissioning and operational phases. Global and local χ^2 minimization algorithms will refine sensor positioning, enhancing accuracy and ensuring optimal detector performance.

In the current detector design, simulations have demonstrated the ideal performance of the detector; however, in practical applications, it is necessary to consider the typical deformation mode as shown in Figure 4.18. The deformation includes elliptical deformation; irregular, wavy distortion; circular distortion with uniform radial expansion.

These deformation modes can affect the detector's ability to determine the relative positions of collision products as they pass through the vertex detector, ultimately impacting the accuracy of the reconstructed collision parameters d_0 and z_0. The effect of each of these deformations was studied in the simulation by modifying the position of the hits according to the three types of deformation. In particular, for each simulated

Draft v0.3.1

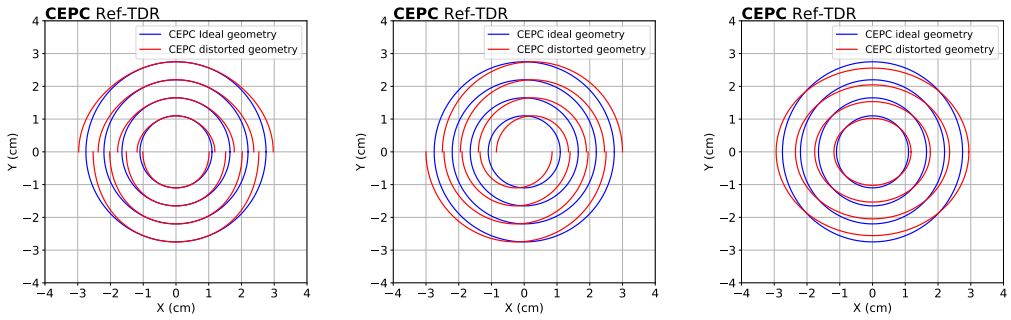

Figure 4.18: Illustration of the hit positions in the transverse plane with ideal vertex geometry and three deformed geometry. The amount of deformation is amplified with respect to the expected one for visualisation. Left Figure: elliptical deformation. The red distorted geometry is elongated horizontally, demonstrating a deformation primarily along the x-axis. Middle Figure: Illustration of the hit positions in the transverse plane for vertex geometry exhibiting irregular, wavy distortion. The distorted geometry has noticeable undulations, indicating non-uniform deformation affecting both the x and y directions unevenly. Right Figure: Illustration of the hit positions in the transverse plane for vertex geometry showing a circular distortion with uniform radial expansion. The distorted geometry presents a uniformly increased radius, representing an isotropic deformation compared to the ideal geometry.

charged-particle trajectory, the intersection with the deformed geometry was computed to determine the corresponding position of the hit in the local detector coordinates. The track-reconstruction algorithm was then executed assuming an ideal geometry to quantify the effect of the detector deformations in the absence of a detector alignment procedure.

4.4.3 Real-time monitoring

A laser-based online alignment monitoring system will perform real-time checks, verifying alignment accuracy continuously.

Due to the air cooling design in the vertex detector, it is important to monitor the movement of the MAPS sensors. Inspired by the laser alignment system of CMS experiment [12], it is proposed to install laser alignment system to keep track of these movement. In Figure 4.19, a laser source placed on the right side of the 4th layer of chips is used to monitor the movement of the first layer of MAPS; laser sources are placed on the service portions on both sides to monitor the movement of the 3rd, 2nd and 1st layer of MAPS. This system utilizes near-infrared laser beams (1050 nm) directed through the vertex detector to detect potential movements or deformations of the mechanical structure. Laser sources located in service areas are triggered to send pulsed infrared light to MAPS sensors of the vertex detector. By detecting their interaction with the silicon sensors, the system can infer movements of the MAPS sensors, ensuring that any deformations due to environmental factors like temperature, air flow, or magnetic fields are promptly identified.

Draft v0.3.1

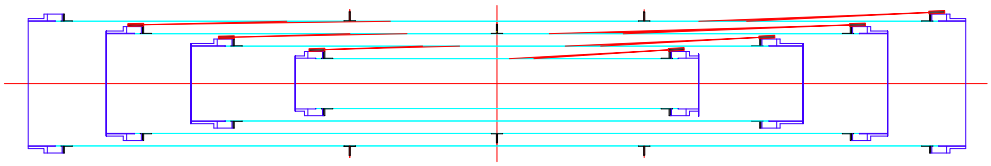

Figure 4.19: A laser-based online alignment monitoring system. Red lines diagonally connect with the aqua blue line (MAPS chip) are the lasers, and the laser sources are placed at both sides of the inner three layers and right side of the 4th layer to monitor the movement of each layer.

To validate the laser calibration system, signals generated by the laser were simulated using Geant4 [13] within the CEPC Software (CEPCSW) framework. The laser was emitted as a point source from the position (13 mm, 0, -85 mm), directed at an angle of $\theta = 10^\circ$ and $\phi = 0$. In the absence of a focusing system, a divergence of $\tan\alpha = 0.1$ was established.

The resulting laser beam spot on the second layer of the vertex detector is presented in Figure 4.20.

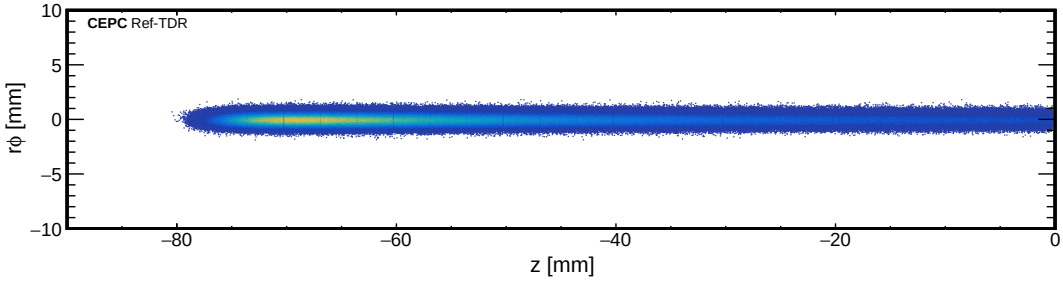

Figure 4.20: The laser beam spot on the second layer from (13 mm, 0, -85 mm) in cylindrical coordinate system, where the horizontal axis is the z-coordinate, and the vertical axis is the $r\phi$ coordinate. And each region is divided by a blank or lower rate than its neighbor means one sensor.

When simulating deformation by radially displacing the second layer outward by $d = 10\mu\text{m}$, the resulting distribution of signal IDs, The observed difference of 2 corresponds to a distance of $50\mu\text{m}$, which is consistent with relationship $d/\tan\theta \approx 57\mu\text{m}$. If an accurate fitting function can be employed to characterize this distribution and precisely determine the most probable position, it would enable more accurate detection of displacement. These findings indicate that the laser calibration system can infer positional changes through the distribution of pixel IDs.

4.5 R&D efforts and results

To meet the stringent requirements of high spatial resolution, low material budget, rapid readout speeds, and low power consumption, significant efforts have been directed to-

Draft v0.3.1

ward advancing MAPS technologies, notably through the TaichuPix and JadePix projects.

The JadePix project focuses on investigating CMOS pixel sensors for the CEPC vertex detector, exploring low-power readout schemes. Concurrently, the TaichuPix series is dedicated to developing MAPS featuring advanced in-pixel electronics optimized for rapid readout. These sensors utilize a data-driven, column-drain architecture specifically designed to meet the fast response requirements imposed by the high collision rates at CEPC.

4.5.1 CMOS pixel sensor JadePix series

The CEPC vertex detector imposes stringent requirements on spatial resolution. To achieve a spatial resolution of 3 μm, the pixel size needs to be reduced to less than 20 μm, which is limited by the feature size of integrated circuit technology. JadePix utilizes a specialized 180 nm CMOS integrated circuit process optimized for ionizing radiation detection, which is a modification and development based on the commercial CMOS Imaging Sensor process. The pixel pitch in this process typically ranges from 25 to 30 μm. Therefore, the key focus of JadePix's development is on how to reduce the pixel size while also meeting the requirements for low power consumption and fast time stamping.

4.5.1.1 Overview of JadePix development

The JadePix series of chips are primarily designed and optimized for high spatial resolution, low power consumption, and fast time stamping. Since 2015, a total of 5 chips have undergone continuous improvements which are shown as Table 4.12.

Table 4.12: Overview of JadePix development

Chip Name	Pixel Array	Pixel Pitch(μm^2)	Analog Front-end	Matrix Readout	Design Team
JadePix-1	128×192, 160×96	16×16, 33×33	Source follower	Rolling Shutter	IHEP
JadePix-2	96×112	22×22	Diff. Amp., CS Amp.	Rolling Shutter	IHEP
JadePix-3	512×192	16×23, 16×26	ALPIDE	Rolling Shutter	IHEP, CCNU, SDU, DLNU
JadePix-4	356×489	20×29	ALPIDE	AERD	CCNU, IHEP
JadePix-5	896×480	20×30	ALPIDE	AERD	IHEP, CCNU

JadePix-1[14] primarily focused on sensor optimization, comparing different geometric dimensions [15] and providing experimental evidence for the design of small charge collection electrodes [16]. As Figure 4.21 shows, the optimal spatial resolution obtained through beam tests on a $33 \times 33 \mu m^2$ pixel array was $2.7 \mu m$ [17].

Draft v0.3.1

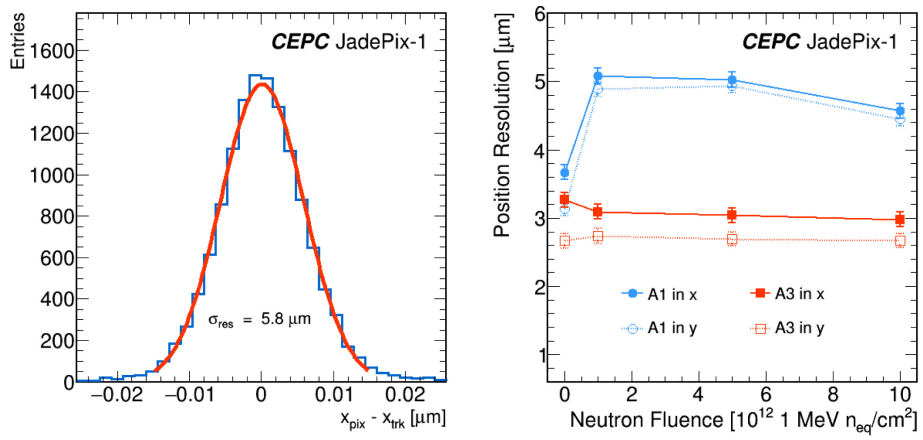

(a) (b)

Figure 4.21: (a) Residual distribution of JadePix-1 sensor in the x direction; (b) position resolution for sensors with a small electrode (A1) and a large electrode (A3) before and after the neutron irradiation.

JadePix-2 investigated AC coupling and different analog front-end amplifiers [18], attempting to optimize resolution, power consumption, and time stamping design using a 180 nm process based on the Minimum Ionising MOS Active pixel sensor (MIMOSA) architecture.

JadePix-3 utilized the low-power front-end amplifier of ALICE Pixel Detector (ALPIDE)[4], combined with a Rolling Shutter readout architecture, achieving the smallest pixel design among similar chips at $16 \times 23 \mu m^2$. Infrared laser tests showed spatial resolutions of 3.4 μm (X-direction) and 2.7 μm (Y-direction) [19]. A 5-layer beam telescope system was constructed based on this chip, measuring spatial resolutions on a 5.8 GeV electron beam of 5.2 μm (X-direction) and 4.6 μm (Y-direction) [20] . The cluster size from beam tests was significantly larger than that from laser tests, adversely affecting the spatial resolution. The highest efficiency reached 99 % at the optimum threshold of 160 e^-.

JadePix-4 and JadePix-5 employed ALPIDE analog front-ends and AERD readout architectures. The latter is an efficient sparse readout logic that can quickly read out the addresses of hit pixels at very low power consumption and apply time stamps around the periphery of the pixel array. The AERD readout architecture has been adopted not only by various CMOS pixel chips on the 180 nm process but also by the next-generation 65 nm Stitching process.

4.5.2 MAPS TaichuPix series

In order to address the high hit density of the CEPC, a MAPS, named TaichuPix, has been developed with the goal of high readout speed and high spatial resolution. TaichuPix-1[7] and TaichuPix-2[8], are multi-project wafers, and TaichuPix-3 is a full-scale prototype with an engineering run. The pixel matrix of TaichuPix-3 is 1024×512 with a pixel pitch

Draft v0.3.1

of 25 μm, and a thickness of 150 μm. The proposed baseline vertex detector consists of three layers of ladders, with double-sided mounted TaichuPix-3 sensors.

Each pixel of the TaichuPix-3 chip integrates a sensing diode, an analog front-end, and a digital logical readout in each pixel. The analog front-end is designed based on the ALPIDE[4] chip, which is developed for the upgrade of the ALICE ITS[3]. In order to address the high hit rate of CEPC, the analog front-end of TaichuPix-3 has been specifically optimized to ensure a quicker response. In addition, the digital logical readout includes a hit storage register, logic for pixel mask, and test pulse configuration. The digital logical readout follows the FE-I3[21] designed for the ATLAS pixel detector, but it has been modified to adjust the pixel address generator and relocate the timestamp storage from within the pixel to the end of the column. This modification was necessary due to pixel size constraints. Furthermore, the double-column drain peripheral readout architecture of the TaichuPix-3 chip employs an address encoder with a pull-up and pull-down network matrix.

4.5.2.1 TaichuPix specification and performance

Specification Table 4.13 summarizes the design specifications of the TaichuPix-3 chip. The performance of the pixel sensor chip has been verified with a 4 GeV electron beam at Deutsches Elektronen-Synchrotron (DESY) II. The intrinsic spatial resolution was found to be $4.8\mu\mathrm{m}$ and $4.5\mu\mathrm{m}$, and the detection efficiency reached 99 %, which meet the requirements.

Table 4.13: Design specifications of the TaichuPix-3 chip.

Specification	Index
Pixel size	$25 \times 25\mu\mathrm{m}^2$
Dimension	$15.9 \times 25.7\mathrm{mm}^2$
Techonology	CIS 180nm
Dead time	$< 500\mathrm{ns}$
Power density	$< 200\mathrm{mW} \cdot \mathrm{cm}^{-2}$
Max. Hit rate	$36 \times 10^6 \mathrm{cm}^{-2} \cdot \mathrm{s}^{-1}$

In order to verify the performance of TaichuPix, we conducted multiple beam tests at DESY II[9].

Spatial resolution The spatial resolution of TaichuPix-3 chips are verified by electron beam provided by DESY II. The intrinsic spatial resolution is derived from an unbiased distribution of tracking residual, which excludes the Device Under Test (DUT). The scattering angle is predicted using Highland formula.

Draft v0.3.1

After considering the contribution from track resolution, the intrinsic spatial resolution for TaichuPix-3 chip is about $5\mu\mathrm{m}$. Figure 4.22 show the spatial resolution as a function of threshold. In general, a higher threshold leads to a smaller cluster size, which introduces a bias in estimating the actual hitting position and ultimately worsens the intrinsic resolution. As depicted in Figure 4.22, for the two DUTs, increasing the threshold results in a deterioration of the intrinsic resolution. However, for DUT$_B$, a worse resolution is also observed when the threshold is lower than $\xi_B = 218\ e^-$, which can be attributed to the increased noise at the lower thresholds. The best resolution for DUT$_A$ is 4.72 ± 0.13 (syst.) μm in the x-direciton, 4.83 ± 0.10 (syst.) μm in the y-direciton when $\xi_B = 265\ e^-$. For DUT$_B$, the best resolution is 4.46 ± 0.13 (syst.) μm int the x-direciton, 4.52 ± 0.13 (syst.)μm int the y-direciton when $\xi_B = 218\ e^-$.

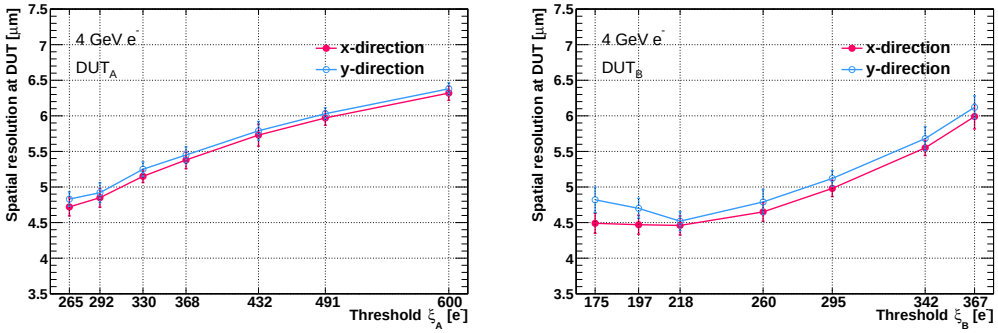

(a) **(b)**

Figure 4.22: Spatial resolution as a function of threshold for DUT$_A$(a) and DUT$_B$(b) in the x-direction and y-direction. The error bars represent the total systematic uncertainty.

Detection efficiency The maximum detection efficiency is 99.76 % for DUT$_B$ and 99.68 % for DUT$_A$. However, the efficiency of DUT$_B$ drops significantly at high thresholds compared to DUT$_A$. This can be explained by the difference in the process of the two DUTs. Comparing to DUT$_B$, DUT$_A$ has an additional low-dose N-layer, which enables a larger depletion of the epitaxial layer and results in a larger charge collection area.

4.5.2.2 Prototype of a planar CMOS vertex detector

In striving to fulfill requirements in Table 4.13, a planar CMOS vertex detector prototype (shown as Figure 4.23) has been developed and evaluated[22] using an electron beam from DESY II.

Draft v0.3.1

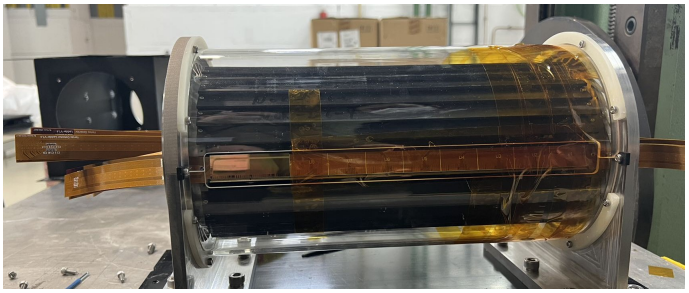

Figure 4.23: Planar vertex detector prototype with six ladders mounted for beam test.

Spatial resolution and detection efficiency The spatial resolution is derived from an unbiased distribution of tracking residual obtained using the GBL track-fitting algorithm, which excludes the DUT. The scattering angle is predicted using the Highland formula. After alignment, the standard deviation for $\mathrm{DUT_A}$ and $\mathrm{DUT_B}$ at minimum threshold is approximately 5.4 $\mu\mathrm{m}$ and 5.0 $\mu\mathrm{m}$, respectively. Additionally, the spatial resolution of both DUTs deteriorates as the threshold increases, and due to reduced charge-sharing effects on $\mathrm{DUT_A}$, it exhibits poorer resolution compared to $\mathrm{DUT_B}$. At the lowest threshold setting, the best spatial resolution achieved is 5.38 ± 0.12 (syst.)$\mu\mathrm{m}$ in the u-direction and 5.52 ± 0.10 (syst.)$\mu\mathrm{m}$ in the v-direction for $\mathrm{DUT_A}$, and 4.97 ± 0.08 (syst.)$\mu\mathrm{m}$ in the u-direction and 5.21 ± 0.08 (syst.)$\mu\mathrm{m}$ in the v-direction for $\mathrm{DUT_B}$. To demonstrate the overall performance of the prototype, the measured spatial resolution in this article involves the resolution of the reference tracks.

The efficiencies of $\mathrm{DUT_A}$ and $\mathrm{DUT_B}$ exhibit a decreasing trend as the threshold increases. The best detection efficiency is 99.3 % and 99.6 % for $\mathrm{DUT_A}$ and $\mathrm{DUT_B}$, respectively.

Air cooling The vertex detector is designed for very high spatial resolution. For air cooling, in addition, to cool the detector to a certain temperature, one needs to consider the vibration amplitude caused by the forced airflow, which should not affect the expected high spatial resolution. This issue was noted and studied during the prototype R&D phase. The test results, indicate that even under a higher airflow rate of 4 m/s, the maximum amplitude of vibration of the ladder support is less than 1.9 $\mu\mathrm{m}$. In addition, during the beam test of the VTX prototype, air cooling with a fan was employed, which decrease the chip temperature from $41°\mathrm{C}$ to $25°\mathrm{C}$ at a power dissipation of approximately $60\mathrm{mW/cm^2}$, and no impact on the spatial resolution was observed. The strategy for addressing vibration in the baseline design of the vertex detector is similar to that of previous studies; prototyping the key structural elements and conducting related tests later on is the preferred method.

Draft v0.3.1

4.5.2.3 Prototype of a stitching CMOS detector

A stitched CMOS pixel sensor has been developed. It was designed and fabricated in a 0.35 μm technology, which provides a thickness of 14 μm epitaxial layer and four metal layers for routing. Since there are triple wells in this process, only NMOS could be used in the pixel. The total pixel array is 644 rows and 3600 columns stitched by a basic pixel array of 92 rows and 600 columns. It works in a rolling shutter readout mode. As a full functional prototype, it integrated column-level discriminator, on-chip zero suppression, interface circuits such as bias DAC, analog buffers, Inter-Integrated Circuit (I2C) control, Phase-Locked Loop (PLL), Low-Voltage Differential Signaling (LVDS), Low Dropout Regulator (LDO), etc. The total area is up to $11 \times 11\text{cm}^2$. In order to study charge collection efficiency and charge sharing, each basic pixel array has six submatrices with different pixel sizes and diode arrangements. The prototype chip is being tested and its development could provide experience in developing stitched sensor with advanced technology.

The radius bending test We have conducted studies on vertex detector with stitching technology. Dummy wafers have been used for bending tests, prototype manufacturing, and, meanwhile, small-area MAPS chips were used to study the impacts of bending on the chip performance.

Silicon is a brittle material. It undergoes an irreversible brittle fracture when the stress exceeds its compressive strength. We thinned the wafers to thicknesses of 30 μm, 40 μm, and 50 μm, and successfully completed bending tests with and without a film, as well as fatigue tests for different radii in various sequences, . Currently, the bending limit test has successfully achieved a minimum bending radius of 12 mm , as shown in Figure 4.24a. Additionally, we performed over 20 times of bending-recovery-bending tests on the same wafer. The prototype in Figure 4.24b has been placed for over 2 years without damage.

Draft v0.3.1

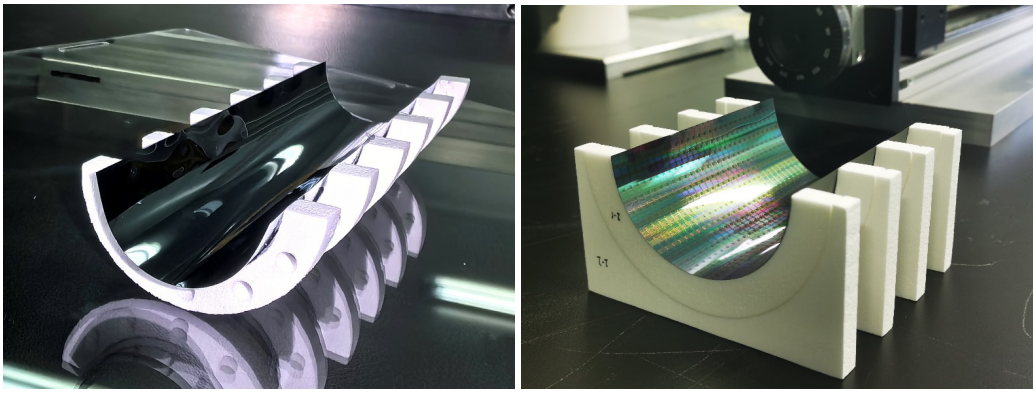

(a) **(b)**

Figure 4.24: Prototype for bending test. (a) Testing of bending limit, the minimum bending radius of 12 mm has achieved. (b) Determining the damage-free duration of the bending wafer, this prototype placed for over 2 years without damage.

4.6 Performance

4.6.1 Hit number and efficiency

Due to the assembly of modules using sensors, which in turn form ladders or semi-circles, there inevitably exist some dead zones that cannot be used for detection, such as data interface block, switches, periphery, bias as shown in Figure 4.9. When charged particles pass through these regions, no signal output will be obtained, meaning that part of the hits along this trajectory will be lost. During layout optimization, different deflections in the phi direction have been applied to different layers with the aim of avoiding these dead zones, thereby preventing the loss of multiple hits from a single trajectory. Furthermore, for planar Taichu technology, the width of the ladders has been increased to avoid empty sensor regions in the phi direction. However, when the width becomes too large, it could lead to a situation where both adjacent ladders at the same layer have signals, which increases the material volume of the overlapping area. To assess the reasonableness of the dead zones and overlaps, simulations using chargedgeantino were performed to obtain the number of hits in the vertex detector.

The Tracklet Efficiency is defined as the sum of hits left by all chargedgeantinos' simulated trajectories passing through the vertex detector with a hit count greater than or equal to 4, divided by the total number of expected layers (6) that the vertex detector is expected to be traversed by all simulated events. This can be expressed mathematically as:

$$\text{Tracklet Efficiency} \quad = \quad \frac{\sum_i^N \text{Hits}i^{(\geq 4)}}{N \times L} \tag{4.1}$$

where $\text{Hits}i^{(\geq 4)}$ represents the number of hits left by the i-th chargedgeantino's simulated trajectory passing through the vertex detector with a hit count greater than or equal to 4,

Draft v0.3.1

N is the total number of simulated events, and L is the expected number of layers that the vertex detector is expected to be traversed (in this case, 6). As shown in Figure 4.25a, for a chargedgeantino with a momentum of 20 GeV, the particle's tracklet efficiency is 99.635% at $\theta = 60°$. When each track is required to pass through the first layer of the vertex detector, the tracklet efficiency is 96.75%.

Figure 4.25b illustrates the tracklet efficiency and its errors for 20 GeV chargedgeantino particles passing through the baseline vertex detector at different polar angles. The tracklet efficiency is consistently close to 100% in all cases.

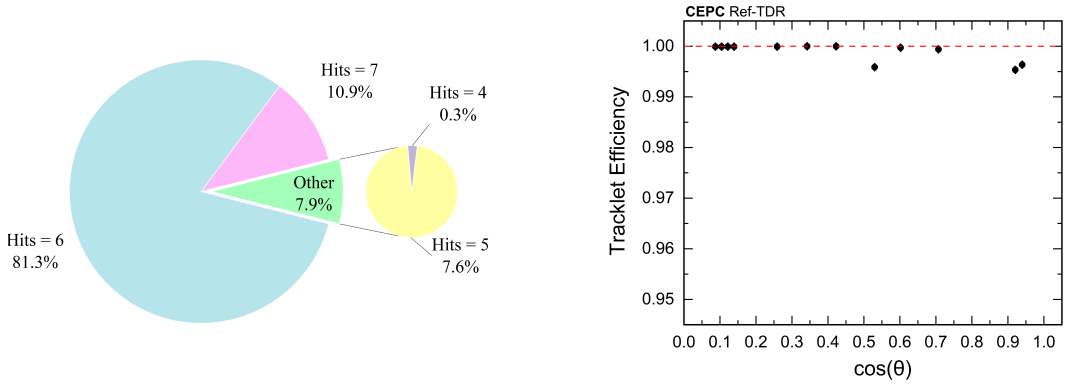

(a) **(b)**

Figure 4.25: Performance on tracking. (a) Each track includes the percentage of hits when the number of hits is 4, 5, 6, and 7, based on the simulation of 10,000 chargedgeantino particles by the vertex detector at $\theta = 20°$ and 20 GeV. (b) Tracklet efficiency and its errors for 10000 chargedgeantino particles at 20 GeV, originating from (0, 0, 0) and passing through the vertex detector at different polar angles.

4.6.2 Resolution

The vertex detector design described in Section 4.1.2 will serve as the the baseline schemes in the following sections. Additionally, we propose a backup scheme, which utilizes the same materials as PVTX5-6 in the baseline scheme to construct PVTX1-2 and PVTX3-4. The specific dimensions and material quantities of the backup scheme are detailed in Table X. Simulations were performed using CEPCSW in conjunction with the remaining sub-detectors of the Track system, with μ^- as the outgoing particles and a conservative single-point resolution of 5μm assumed for the chip. Through simulation results, as shown in Figure 4.26, the baseline scheme demonstrates its superior d_0 resolution performance among the two schemes.

Draft v0.3.1

Table 4.14: Geometric configuration parameters. PVTX is used to denote the layer of VTX employing a planar CMOS sensor.

PVTX X	radius [mm]	length [mm]	height [mm]	support thickness [μm]
PVTX 1-2	12.46	260.0	1.7	334
PVTX 3-4	27.89	494.0	2.5	358
PVTX 5-6	43.79	749.0	3.2	370

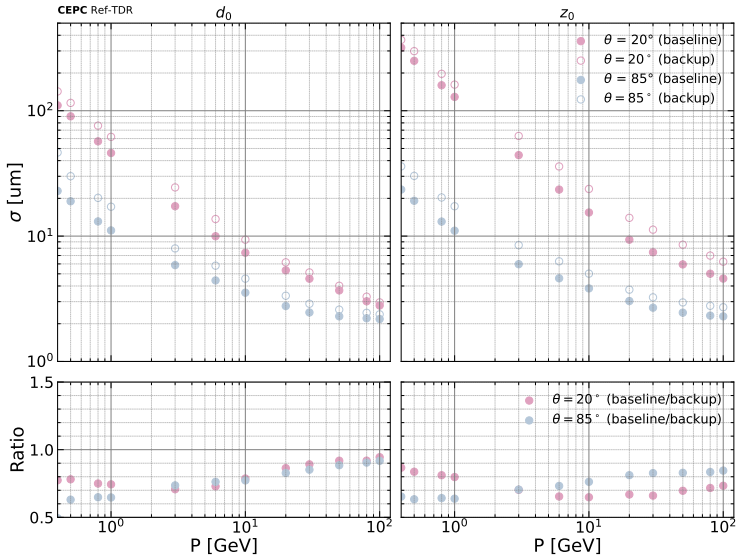

Figure 4.26: The resolution of the impact parameter d_0 and z_0 in the two schemes varies with the change in the momentum of the outgoing particles.

As previously demonstrated during the optimization, the adoption of the low-mass stitching technique allows the baseline scheme of the vertex detector to achieve good resolution of the impact parameter d_0 of tracks even at high momentum, as well as improved d_0 resolution at low momentum. In fact, not only the d_0 resolution, but the baseline scheme also exhibits excellent performance for the resolution of impact parameter z_0, as shown in Figure 4.26. The simulation results demonstrate that the trend of the z_0 resolution as a function of momentum is analogous to that of d_0, with only minor discrepancies observed. This observation aligns with the utilization of pixel detectors in the vertex detector, where the precision of z position measurements is equivalent to that of $r\phi$ measurements. Such findings indicate that when comparing different configurations, focusing exclusively on d_0 resolution is a valid approach that also minimizes the workload. The results indicate that an increase in momentum correlates with an enhancement in resolution. This improvement can be attributed to the pronounced effects of multiple scattering in material at low momentum. Similarly, as the polar angle θ diminishes, the amount of material traversed by charged tracks increases proportionally to $\sim 1/\sin\theta$, which further amplifies the multiple scattering effects and leads to a degradation in resolution.

Similarly, the z_0 resolution of the backup scheme in Figure 4.26 is also slightly worse

Draft v0.3.1

than of the baseline scheme.

4.6.3 Performance under sensor failure scenarios

In addition to the previously mentioned impact of dead zones on performance, during actual operation, the background of the beam may suddenly increase in intensity for a short period of time especially at the initial stages of accelerator operation when the state has not yet been optimized and adjusted, resulting in some vertex detector units failing to operate normally. Furthermore, during operation, it is also possible for certain units to become damaged. When such situations arise, the performance of the vertex detector is bound to decline. However, to ensure the smooth progress of physical analysis, the design of the vertex detector must guarantee that even in the worst-case scenarios, the performance does not experience a dramatic drop.

To this end, in the simulation process, we assume that a certain layer of the vertex detector does not produce signals to estimate performance under this special circumstance. As shown in Figure 4.27, the estimated performance for normal conditions and for damages from the first to the sixth layers is presented. It is evident that the current vertex detector scheme can ensure that, in the case of a single layer loss, the performance decrease does not exceed 30 %, with the loss of the first layer having the most significant impact. For cases of individual unit damage, the overall performance can be viewed as a weighted average of the probabilities of the intact and damaged sections. Considering the very low likelihood of two layers being damaged simultaneously, it can be reasonably anticipated that the overall impact will be minimal.

Draft v0.3.1

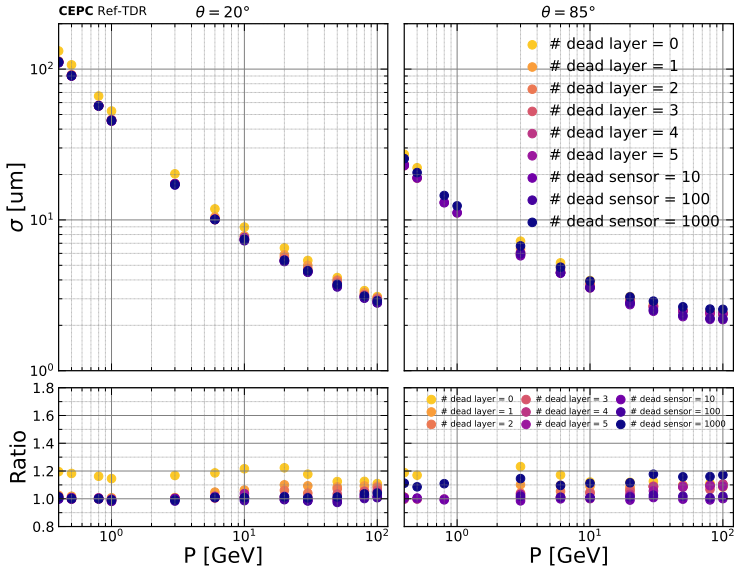

Figure 4.27: Resolution of the impact parameter d_0 of tracks obtained by the baseline vertex detector under different conditions of dead layers/sensors, respectively inactive the first (0), second(1), third(2), fourth(3), fifth(4), sixth(5) whole layer or total 10, 100, 1000 sensors in all layers in simulation.

4.6.4 Performance with beam background

In addition, due to the proximity of the vertex detector to the beam pipe, it is crucial to evaluate the effects of beam background on its performance during the design phase.

This approach incorporates true simulated backgrounds into the signal, as outlined in Section **??**. This method facilitates a comparison of the d_0 resolution before and after background incorporation, as illustrated in Figure 4.28, where no discernible effects are observed. Thus, it is evident that provided the levels of beam background remain consistent with those determined in current simulation studies, the vertex detector is poised to deliver outstanding performance. Nonetheless, it should be noted that the inclusion of beam background may lead to increased processing time for track reconstruction. Therefore, subsequent efforts should focus on algorithm optimization and enhanced computational efficiency to mitigate this increase.

Draft v0.3.1

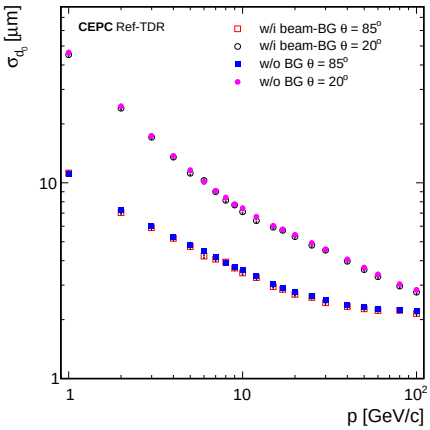

Figure 4.28: Comparison of resolution of the impact parameter d_0 of tracks between clean single muon signal (w/o BG) and mixing beam background (w/i beam-BG) at polar angle of $85°$ and $20°$.

4.7 Summary and future plan

The MAPS-based detector layout consists of 6 cylindrical layers of pixel sensors with pixel sizes in the order of $25\ \mu\text{m} \times 25\ \mu\text{m}$, enabling hit resolutions better than $5\ \mu\text{m}$. The inner four layers are bent MAPS cylinders. The outer two layers are based on double-side ladder technology.

Initial vertex detector prototypes using double-side ladder technology have demonstrated a spatial resolution better than $5\ \mu\text{m}$ with air cooling in DESY testbeam. Geant4-based simulations, demonstrate that the baseline design of vertex detector can achieve the target impact parameter resolution.

Future R&D priorities include:

1. Development of wafer-scale stitching MAPS sensors.
    - Initially, the stitching chip will leverage mature 180 nm technology (e.g., TowerJazz) to keep R&D risks and costs within reasonable bounds. The pixel cell and matrix design will build on the proven architecture of previous prototype chips, with focused efforts on stitching-related challenges and ensuring basic cell designs draw from verified experience.
    - The second-generation stitching chip will transition to 65 nm/55 nm technology, with potential candidates including TPSCO's 65 nm technology and domestic HLMC's 55 nm technology. Synergy with sensor development for future LHC upgrades is anticipated.
2. Ultra-thin mechanical supports and low-mass integration techniques.
    - The plan begins with exploring the construction of a mock-up featuring dummy heaters for thermal performance testing. Results will also validate thermal simulation models.

Draft v0.3.1

3. Construction of a full-scale vertex detector prototype to address challenges in mechanical precision, cooling performance, and system-level integration.

References

[1] L. Greiner et al. "A MAPS based vertex detector for the STAR experiment at RHIC". In: *Nuclear Instruments and Methods in Physics Research Section A: Accelerators, Spectrometers, Detectors and Associated Equipment* 650.1 (2011). International Workshop on Semiconductor Pixel Detectors for Particles and Imaging 2010, pp. 68–72. ISSN: 0168-9002.

[2] C. Hu-Guo et al. "First reticule size MAPS with digital output and integrated zero suppression for the EUDET-JRA1 beam telescope". In: *Nuclear Instruments and Methods in Physics Research Section A: Accelerators, Spectrometers, Detectors and Associated Equipment* 623.1 (2010). 1st International Conference on Technology and Instrumentation in Particle Physics, pp. 480–482. ISSN: 0168-9002.

[3] F. Reidt. "Upgrade of the ALICE ITS detector". In: *Nuclear Instruments And Methods In Physics Research Section A: Accelerators, Spectrometers, Detectors And Associated Equipment* 1032 (2022), p. 166632.

[4] M. Mager. "ALPIDE, the Monolithic Active Pixel Sensor for the ALICE ITS upgrade". In: *Nuclear Instruments And Methods In Physics Research Section A: Accelerators, Spectrometers, Detectors And Associated Equipment* 824 (2016). Frontier Detectors for Frontier Physics: Proceedings of the 13th Pisa Meeting on Advanced Detectors, pp. 434–438.

[5] The ALICE collaboration. *Technical Design report for the ALICE Inner Tracking System 3 - ITS3 ; A bent wafer-scale monolithic pixel detector*. Co-project Manager: Magnus Mage, magnus.mager@cern.chds. CERN, 2024.

[6] J. Liu. "A truly cylindrical vertex detector based on bent, wafer-scale stitched CMOS sensors". In: *Nuclear Instruments And Methods In Physics Research Section A: Accelerators, Spectrometers, Detectors And Associated Equipment* 1064 (2024), p. 169355.

[7] T. Wu et al. "The TaichuPix1: a monolithic active pixel sensor with fast in-pixel readout electronics for the CEPC vertex detector". In: *Journal Of Instrumentation* 16 (2018), pp. 164–172.

[8] X. Wei et al. "High data-rate readout logic design of a 512 × 1024 pixel array dedicated for CEPC vertex detector". In: *Journal Of Instrumentation* 14 (2012). C1 (2019,12).

[9] T. Wu et al. "Beam test of a 180nm CMOS Pixel Sensor for the CEPC vertex detector". In: *Nuclear Instruments And Methods In Physics Research Section A: Accelerators, Spectrometers, Detectors And Associated Equipment* 1059 (2024), p. 168945.

[10] Xiaomin Wei on behalf of the CEPC MOST2 vertex detector design team. "Design of a fast readout CMOS pixel sensor for the first prototype of CEPC Vertex Detector". In: *IEEE Real Time Conference*. Quy Nhon, Vietnam, 2024.

[11] Jinyu Fu et al. "Mechanical design of an ultra-light vertex detector prototype for CEPC". In: *Radiation Detection Technology and Methods* 6.2 (2022), pp. 159–169. ISSN: 2509-9930.

[12] Bruno Wittmer et al. "The laser alignment system for the CMS silicon microstrip tracker". In: *Nuclear Instruments and Methods in Physics Research Section A: Accelerators, Spectrometers, Detectors and Associated Equipment* 581.1 (2007). VCI 2007, pp. 351–355. ISSN: 0168-9002.

[13] S. Agostinelli et al. "Geant4—a simulation toolkit". In: *Nuclear Instruments and Methods in Physics Research Section A: Accelerators, Spectrometers, Detectors and Associated Equipment* 506.3 (2003), pp. 250–303. ISSN: 0168-9002.

[14] L. Chen et al. "Characterization of the prototype CMOS pixel sensor JadePix-1 for the CEPC vertex detector". In: *Journal Of Instrumentation* 14 (). C05023 (2019,5).

Draft v0.3.1

[15] Ying Zhang et al. “Charge collection and non-ionizing radiation tolerance of CMOS pixel sensors using a 0.18μm CMOS process”. In: *Nuclear Instruments and Methods in Physics Research Section A: Accelerators, Spectrometers, Detectors and Associated Equipment* 831 (2016). Proceedings of the 10th International “Hiroshima” Symposium on the Development and Application of Semiconductor Tracking Detectors, pp. 99–104. ISSN: 0168-9002.

[16] L. J. Chen et al. “Characterization of the first prototype CMOS pixel sensor developed for the CEPC vertex detector”. In: *Radiation Detection Technology and Methods* 3.3 (2019), p. 45. ISSN: 2509-9949.

[17] Y. Han et al. “Test beam measurements of an irradiated prototype pixel sensor designed for the CEPC vertex detector”. In: *Nuclear Instruments and Methods in Physics Research Section A: Accelerators, Spectrometers, Detectors and Associated Equipment* 977 (2020), p. 164267. ISSN: 0168-9002.

[18] Yang Zhou et al. “Highly compact digital pixel structures developed for the CEPC vertex detector”. In: *Nuclear Instruments and Methods in Physics Research Section A: Accelerators, Spectrometers, Detectors and Associated Equipment* 980 (2020), p. 164427. ISSN: 0168-9002.

[19] Sheng Dong et al. “Design and characterisation of the JadePix-3 CMOS pixel sensor”. In: *Nuclear Instruments and Methods in Physics Research Section A: Accelerators, Spectrometers, Detectors and Associated Equipment* 1048 (2023), p. 167967. ISSN: 0168-9002.

[20] Sheng Dong et al. “Performance study of the JadePix-3 telescope from a beam test”. In: *Nuclear Instruments and Methods in Physics Research Section A: Accelerators, Spectrometers, Detectors and Associated Equipment* 1065 (2024), p. 169551. ISSN: 0168-9002.

[21] I. Perić et al. “The FEI3 readout chip for the ATLAS pixel detector”. In: *Nuclear Instruments And Methods In Physics Research Section A: Accelerators, Spectrometers, Detectors And Associated Equipment* 565 (2006). Proceedings of the International Workshop on Semiconductor Pixel Detectors for Particles and Imaging, pp. 178–187.

[22] Shuqi Li et al. “Beam Test of a Baseline Vertex Detector Prototype for CEPC”. In: *IEEE Transactions on Nuclear Science* 71.6 (2024), pp. 1319–1323.

Draft v0.3.1

Glossary

AERD Address-Encoder and Reset-Decoder 26, 27
ALICE A Large Ion Collider Experiment 9, 10, 13, 28
ALPIDE ALICE Pixel Detector 10, 13, 26–28

BX Bunch Crossing 9

CEPC Circular Electron Positron Collider 1, 2, 9, 10, 26–28
CEPCSW CEPC Software 25, 33
CERN European Organization for Nuclear Research 9
CFRP Carbon Fiber Reinforced Polymer 5, 18, 19
CIS Cmos Image Sensor 28
CMOS Complementary Metal Oxide Semiconductor 1, 3, 4, 13, 16, 26, 27, 29, 31, 34
CVTX Curved Vertex Layer 3–5

DAC Digital-to-Analog Converter 16, 31
Dcols Double Columns 14
DESY Deutsches Elektronen-Synchrotron 28, 29
DUT Device Under Test 28–30

FIFO First In First Out 14, 15
FPC Flexible Printed Circuit 5, 18–20, 22

I2C Inter-Integrated Circuit 31
IBIAS bias current 16
ITS Inner Tracker System 9, 10, 13, 28

LDO Low Dropout Regulator 31
LRB Left-end Readout Block 5, 11, 15–17
LVDS Low-Voltage Differential Signaling 31

MAPS Monolithic Active Pixel Sensor 1, 2, 4, 9, 18–27, 31, 37
MIMOSA Minimum Ionising MOS Active pixel sensor 27
MOSS MOnolithic Stitched Sensor 10
MOST MOnolithic Stitched sensor with Timing 10

OCT On-Chip Test 15

PCB Printed Circuit Board 17
PLL Phase-Locked Loop 31
PVTX Planar Vertex Layer 3, 4, 6, 33, 34

Draft v0.3.1

RHIC Relativistic Heavy Ion Collider 9

RPB Right-end Power Block 5, 11

RSU Repeated Sensor Unit 4–6, 11, 12, 15–17

STAR Solenoidal Tracker at RHIC 9

TPSCo Tower Partners Semiconductor Co. 10, 16

VTX Vertex Detector 1, 4, 6–8, 18, 21, 22, 30, 34